



# A Mathematical Model for Outgrowth and Spatial Patterning of the Vertebrate Limb Bud

ROBERT DILLON\* AND HANS G. OTHMER†

\**Department of Mathematics, Washington State University, Pullman, WA 99163, U.S.A. and †Department of Mathematics, University of Utah, Salt Lake City, UT 84108, U.S.A.*

(Received on 1 June 1998, Accepted in revised form on 23 November 1998)

A new model for limb development which incorporates both outgrowth due to cell growth and division, and interactions between morphogens produced in the zone of polarizing activity (ZPA) and the apical epidermal ridge (AER) is developed and analysed. The numerically-computed spatio-temporal distributions of these morphogens demonstrate the importance of interaction between the organizing regions in establishing the morphogenetic terrain on which cells reside, and because growth is explicitly incorporated, it is found that the history of a cell's exposure to the morphogens depends heavily on where the cell originates in the early limb bud. Because the biochemical steps between morphogen(s) and gene activation have not been elucidated, there is no biologically-based mechanism for translating the spatio-temporal distributions of morphogens into patterns of gene expression, but several theoretically plausible functions that bridge the gap are suggested. For example it is shown that interpretation functions based on the history of a cell's exposure to the morphogens can qualitatively account for observed patterns of gene expression. The mathematical model and the associated computational algorithms are sufficiently flexible that other schemes for the interactions between morphogens, and their effect on the spatio-temporal pattern of growth and gene expression, can easily be tested. Thus an additional result of this work is a computational tool that can be used to explore the effects of various mutations and experimental interventions on the growth of the limb and the pattern of gene expression. In future work we will extend the model to a three-dimensional representation of the limb and will incorporate a more realistic description of the rheological properties of the tissue mass, which here is treated as a Newtonian fluid.

© 1999 Academic Press

## 1. Introduction

### 1.1. THE BIOLOGICAL AND BIOCHEMICAL BACKGROUND

Limb development is a model system for the study of tissue growth, pattern formation and differentiation, both from the experimental and

theoretical viewpoints. Limb development in birds (primarily chick), mammals (primarily mouse) and amphibians has been studied extensively for over 70 years, and in chick there is a substantial base of experimental information on which to build mathematical models [reviewed in Maini & Solursh (1991), Tickle & Eichele (1994) and Duprez *et al.* (1996)]. To indicate what a model of the type we develop

E-mail: [dillon@theta.math.wsu.edu](mailto:dillon@theta.math.wsu.edu); [othmer@math.utah.edu](mailto:othmer@math.utah.edu)

must eventually incorporate, we discuss chick limb development in some detail in the remainder of the Introduction. However, the model we present does not incorporate all these details, since much of what is known about spatio-temporal patterns of gene expression in this system is still very qualitative. Thus the model we develop later should be viewed as the first step in an evolutionary process, and one of our long-range objectives is to develop a computational model for growing, deforming tissues in which species are produced and diffuse about. Our aim is to provide a computational tool that can be used to do numerical experiments both on chick limb patterning and in other contexts where growth and patterning occur simultaneously. We begin with a two-dimensional model in this paper, but will extend it to three space dimensions in future work.

In chick, the wing site in the flank of the embryo is determined by Hamburger–Hamilton stage 8 (26–29 hours of incubation\*), the anterior–posterior orientation of the bud is determined by about stage 11 (Hornbruch & Wolpert, 1991), limb outgrowth is visible by stage 17, and the first skeletal element is visible at stage 24. Pattern formation, by which we mean the establishment of spatial differences in gene expression and cell differentiation, is described relative to three axes, the proximo-distal (PD) axis, which extends from somites to wing tip, the anterior–posterior (AP) axis

and the dorsal–ventral (DV) axis [cf. Fig. 1(a)]. The skeletal elements [humerus, radius and ulna, wrist, and digits; cf. Fig. 1(b)] form in a proximal–distal and posterior–anterior sequence. Fate maps show that the anterior half of the limb bud gives rise to part of the humerus, the radius, and digit 2, while the posterior half gives rise to part of the humerus, the ulna, and digits 3 and 4 (Stark & Searls, 1973).

The avian limb bud stems from a thickening of the somatic layer of the lateral plate mesoderm, due to proliferation of mesenchymal cells and perhaps a localized decrease in the cell proliferation rate on either side of the site of future outgrowth (Searls & Janners, 1971; Vogel *et al.*, 1996). In the early stages mesenchymal cells provide the signals to initiate the process of outgrowth, and one or more members of the fibroblast growth factor family (collectively, FGFs, principally FGF-1, FGF-2, FGF-4, and FGF-8) may be a signaling molecule. For example it has been shown that beads soaked with FGF-1, FGF-2 and FGF-4 can induce ectopic limb bud outgrowth when implanted under the ectoderm (Cohn *et al.*, 1995), but more recent evidence suggests that these are not the primary inducers of limb outgrowth *in vivo* [reviewed in Vogel *et al.* (1996)]. *Fgf-8* transcripts are found in the prelimb field before outgrowth in mouse (Crossley & Martin, 1995) and chick (Crossley *et al.*, 1996), and ectopic application of FGF-8 to flank tissue induces ectopic limb formation (Vogel *et al.*, 1996), but *Fgf-10* expression precedes this (Ohuchi *et al.*, 1997). In addition, production of retinoic acid (RA) is high in prospective wing bud tissue (Helms *et al.*, 1994), but whether RA is a

\* The average stage length is 4 hours up to stage 23, and about 6 hours thereafter.

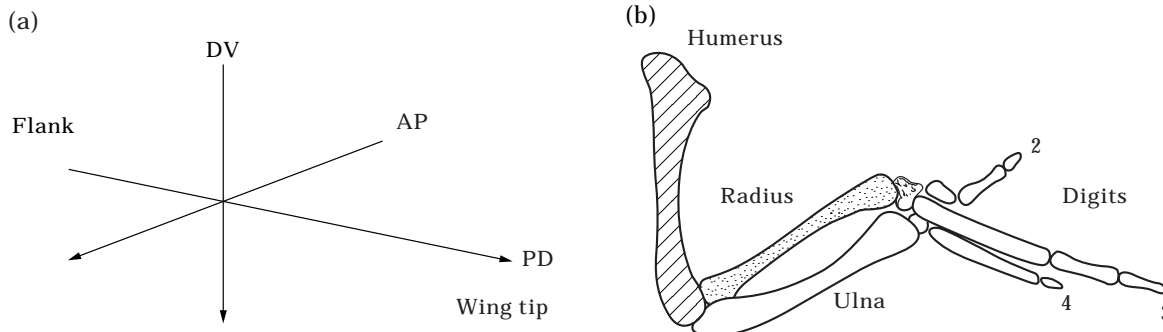


FIG. 1. (a) The orientation of axes used to describe the limb; (b) a schematic of the adult wing skeleton in chick.

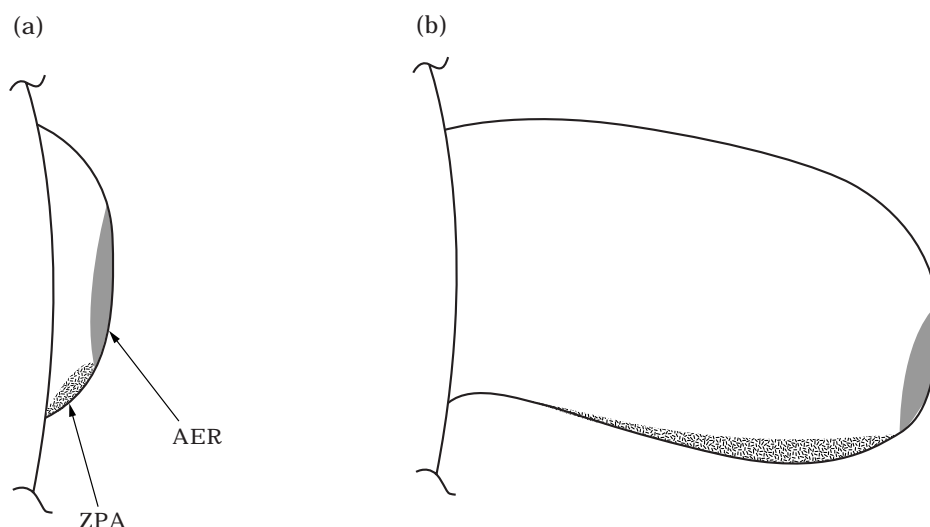


FIG. 2. A schematic of the limb bud, showing the AER and ZPA at (a) approximately stage 18 and (b) stage 25 in chick. At stage 24 the limb is approximately 1 mm long in both the PD and AP directions and 0.5 mm long in the DV direction.

primary inducing molecule or whether it has an effect on cell-cell communication is not understood. Recent evidence (Ogura *et al.*, 1996; Lu *et al.*, 1997) suggests that RA is required for the establishment of the zone of polarizing activity (ZPA), a specialized group of cells that lies at the posterior margin of the limb bud (Zwilling, 1961; Hinchliffe & Griffiths, 1984).

Just as the morphological features can be described relative to three axes, so also can the signaling that is thought to control growth and to determine the spatio-temporal pattern of gene activation. Continued proliferation and outgrowth proximo-distally depends on interactions between the mesenchymal cells and the overlying ectoderm. The ectoderm at the distal tip of the limb bud forms the apical ectodermal ridge (AER), which is apparently determined by the boundary between ectodermal cells which express the factor *radical fringe* and those that do not (Johnson & Tabin, 1997). However early outgrowth of the limb bud and differentiation of the AER are independent, since mutations of the *limb deformity* (*ld*) gene disrupt the latter but not the former (Haramis *et al.*, 1995), but this same mutant shows that localization of the AER is also dependent on dorsal-ventral polarity (Grieshammer *et al.*, 1996; Kuhlman & Niswander, 1997); see also (Niswander, 1997). The dorsal-ventral polarity is itself determined by unknown signals from the somites and the

lateral somatopleure at an earlier stage (Michaud *et al.*, 1997).

In a normal limb the AER does not extend over the entire tip, but occupies only the posterior portion of the tip (cf. Fig. 2). Removal of the AER between stages 18 and 28 stops outgrowth of the limb and leads to a truncated limb with distal skeletal deficiencies (Summerbell, 1974a). Non-AER ectoderm is necessary for growth in pre-stage 16 wing mesenchyme, and ectoderm from either stage 16 or 24 inhibits chondrogenesis in stage 24 mesenchyme (Solursh & Jensen, 1988). The stimulatory effect requires cell contact, whereas the inhibitor is apparently a diffusible molecule. In some of the polydactylous mutants such as *talpid3*, the AER extends across the entire wing tip, and transplants of the mutant mesodermal tissue into a normal ectodermal sleeve induces an anterior extension of the AER and duplication of digits (MacCabe *et al.*, 1975; Wolpert, 1976). The polydactylous mutants produce a limb bud that is wider in the AP direction than normal limb buds, perhaps as a result of the extended AER.

The rapidly dividing mesodermal cells adjacent to the AER form the so-called progress zone (PZ). Recent evidence suggests that a product of the homeobox gene *Msx1* maintains cells in the progress zone in an undifferentiated, rapidly proliferating state, while more proximal cells

begin to differentiate (Robertson & Tickle, 1997). Expression of *Msx1* is regulated by a signal from the AER, probably one of the FGF family. In addition, the bone morphogenetic protein *Bmp-2* is also localized in the AER (at least in mouse) and this may inhibit proliferation (Niswander & Martin, 1993). There is apparently little influence of more proximal tissue on cells in the progress zone, for if the tip of an early limb bud is grafted onto a late stage limb the proximo-distal sequence of skeletal elements appropriate to the tip stage is produced by the graft, while the converse graft produces deletions of proximo-distal elements (Summerbell *et al.*, 1973).

The AER is maintained by a factor produced either in the progress zone or in a specialized group of cells, the zone of polarizing activity (ZPA), that lies at the posterior margin of the progress zone (Zwilling, 1961; Hinchliffe & Griffiths, 1984). At the onset of outgrowth the ZPA is located near the flank on the posterior margin of the bud [Fig. 2(a)], but as outgrowth proceeds the region of maximal ZPA activity moves progressively forward [Fig. 2(b)]. Thus the "ZPA-ness" of tissue depends in part on proximity to the AER. Transplants of the ZPA to the anterior margin of the limb usually lead to duplication of skeletal elements, the pattern of which depends on the location of the transplant relative to the ZPA and the AER (Wolpert, 1987; Tickle *et al.*, 1975). Only cells in the progress zone can respond to the polarizing action of the ZPA (Summerbell, 1974b), and functional gap junctions are required for communication between ZPA cells and anterior mesenchyme, since blocking antibodies to gap junctional proteins prevent ZPA-induced limb duplications (Allen *et al.*, 1990). In light of the fact that ZPA can induce extra digits, one might suppose that the *polydactylous* mutants contain additional ZPA tissue in the anterior part of the limb, but this has been ruled out (Tickle, 1980). Instead it is the response of mesenchymal cells to the normal ZPA signal, rather than the presence of additional ZPA tissue, that is altered in these mutants (Tickle, 1980). In *ld* mutants the

polarizing activity of the ZPA is reduced, the AER cells fail to differentiate into their typical columnar shape, and there are truncations in the autopod region (Haramis *et al.*, 1995).

The polarizing activity of the ZPA is in turn maintained by a factor, probably one of the FGF growth factors, that may be produced in the AER. Removal of posterior AER is followed by a decline in polarizing activity of the ZPA, but the addition of FGF-4 soaked beads to posterior tissue in the absence of the ridge maintains polarizing activity, and outgrowth of the limb bud continues under these conditions (Vogel & Tickle, 1993).

In addition to ectodermal tissue, there are three major cell types present at later stages of limb development: muscle cells, fibroblasts (which form the connective tissue, tendons, etc.) and pre-cartilage cells (chondrocytes). The muscle cells are known to originate in somitic tissue and to then migrate into the limb. However, the chondrocytes and fibroblasts both arise from determination of mesenchymal cells in the progress zone. While the emphasis in the literature is primarily on the spatial pattern of chondrogenesis, it should be kept in mind that the spatial pattern formation problem has two aspects: one is to produce the proper pattern of cartilage anlage, which then lead to the bones, but the other is that the correct spatial pattern of connective tissue must also be produced. If all mesenchymal cells are destined to become fibroblasts, and determination of cells as chondrocytes is merely a derailment of that fate, then the emphasis on the pattern of chondrogenesis is justified. However this has not been demonstrated to date.

## 1.2. POTENTIAL MORPHOGENS AND THEIR INTERACTIONS

Earlier work suggested that retinoic acid (RA) might be a morphogen\* produced in the ZPA (Smith *et al.*, 1989). An implanted bead which releases RA at the anterior margin of the limb produces a digit pattern that is dose-dependent (Tickle *et al.*, 1985): low concentrations lead to a normal digit pattern, higher concentrations produce supernumerary digits, but still higher concentrations lead to wings in which only the humerus and a knob of cartilage are formed.

\* A diffusible substance that induces a concentration-dependent response at some step in the patterning process.

Tickle *et al.* (1985) showed that posterior implants give rise to anterior concentrations high enough to specify an additional digit 2, but despite this the digit pattern is normal. Thaller & Eichele (1987) showed that the concentration of RA *in vivo* is graded in the PA direction. It has been found that there is also a gradient of a cytoplasmic RA-binding protein (CRABP) (Maden *et al.*, 1988) in the AP direction, opposite that of the RA gradient, the net effect of which is to steepen the RA gradient. At present it is also not known whether RA affects gap junctions in chick limb mesenchyme, although it is known to have a biphasic effect in other systems, with enhancement at levels comparable to those found in chick limb (Mehta *et al.*, 1989; Allen *et al.*, 1990). As we noted earlier, recent evidence suggests that RA is required for the establishment of the ZPA (Ogura *et al.*, 1996; Lu *et al.*, 1997).

Currently it is thought that FGF-4 or another member of this family is one of the morphogens. Another is Sonic hedgehog (Shh), a protein secreted by cells in the ZPA. Shh expression is first detected at stage 17, during initiation of limb bud formation (Riddle *et al.*, 1993). Thereafter, Shh expression matches the location of the ZPA as determined by Honig & Summerbell (1985), both in position and in intensity of expression. Sonic is the probable mediator of polarizing activity within the limb bud, because in addition to the fact that its domain of expression colocalizes with the ZPA, Shh is sufficient to convey polarizing activity when misexpressed in the limb bud. Shh may itself be localized near the ZPA, but its range of influence is not unequivocally determined. The “active” N-terminal fragment is tethered to the cell, but other factors may also be involved. In *Drosophila* it has recently been shown that Hh binds to *patched* and a newly-discovered receptor *tout-velu*, which together determine the range of Hh signaling (Bellaïche *et al.*, 1998), and a similar secondary factor may be found in chick limb as well. When applied to the anterior portion of the limb Sonic can induce mirror-image duplications of digits, and Sonic expression can be induced by RA (Riddle *et al.*, 1993). Members of the *Gli* gene family may be involved as downstream mediators of Shh effects, since Shh downregu-

lates *Gli3* and upregulates *Gli1* (Marigo *et al.*, 1996), but little is known about the network of interactions at this level.

There is also strong evidence for interaction between Sonic and FGF-4, either (or both) direct or via intermediaries such as Bmp-2. Some basic observations that suggest this interaction are as follows.

- Sonic hedgehog alone is insufficient to induce expression of Bmp or Hox genes, or mesodermal proliferation in the absence of the AER (Laufer *et al.*, 1994). Sonic hedgehog virus injected into the proximal–medial mesoderm of stage 21 limb buds did not result in ectopic induction of either *Hoxd* genes or Bmp-2, despite the fact that Sonic hedgehog expression was comparable to that seen in distal injections (Laufer *et al.*, 1994).
- The influence of the AER on Sonic hedgehog activity is further demonstrated by the following experiment. The anterior half of the AER was surgically removed in stage 20/21 limb buds, Sonic hedgehog virus was injected into the anterior marginal mesoderm, and the embryos were allowed to develop for an additional 36–48 hours. There was sufficient posterior AER remaining so that embryos developed almost wild-type outgrowth and patterning on the limb bud. In the absence of the AER, Sonic hedgehog does not induce mesodermal proliferation or the expression of *Hox* or Bmp-2 genes. Thus a signal is required from the AER to sustain proliferation and gene induction induced by Sonic hedgehog (Laufer *et al.*, 1994). In the mutants *ld* FGF-4 is not expressed in the AER, and Shh expression is activated but not maintained, which may account for the decrease in polarizing activity (Haramis *et al.*, 1995).
- FGFs promote mesodermal competence to respond to Sonic hedgehog. FGF-4 soaked beads were stapled to AER-denuded anterior mesoderm infected with Sonic hedgehog virus. *Hoxd*-11, *Hoxd*-13 and Bmp-2 expression were induced at expression levels similar to endogenous expression and to expression levels seen in the presence of an AER (Laufer *et al.*, 1994).

To summarize, Sonic hedgehog plays a role in patterning of mesodermal tissue and may regulate FGF-4 expression. FGF-4 induces mesodermal proliferation and maintains Sonic hedgehog expression. Both factors are necessary, because mesodermal tissue can only be patterned by Sonic hedgehog in association with competency provided by FGF-4. Patterning and proliferation are always coincident, and the current model is that FGF-4 from the AER and Sonic hedgehog from the ZPA interact to control the continued outgrowth of the limb bud. However it is possible that exogenously-applied FGF-4 mimics the activity of a different member of the FGF family. In addition, the bone morphogenetic protein Bmp-2 interacts with FGF-4, as is summarized in Fig. 3(a). However, we will not consider the role of Bmp-2 in the first model, and thus we restrict ourselves to the scheme shown in Fig. 3(b).

This is not the complete story, since patterning also occurs along the dorsal-ventral axis. Less is known about this, but it appears that Wnt7a is the primary factor that controls patterning along this axis (Johnson & Tabin, 1997). Thus pattern formation along the three axes of the limb is controlled by a complex network of signaling molecules that originate in the AER, the ZPA and the non-AER ectoderm, and the interactions between these must be understood before a detailed understanding of patterning in the growing three-dimensional limb is possible. However this does not imply that a model based on incomplete information about the gene and morphogen control networks cannot contribute to our understanding of pattern formation.

### 1.3. PREVIOUS MODELS FOR PATTERN FORMATION IN THE LIMB

Wolpert (1969) postulated that the ZPA produces a morphogen which diffuses throughout the tissue and is degraded in it. This would establish a gradient in the PA (posterior-anterior) direction which could provide positional information and could lead to a spatial pattern of differentiation. Tickle *et al.* (1975) estimated that such gradients have to be established within 10 hours across a distance of 500–1000  $\mu\text{m}$ , and concluded that transport by diffusion is fast enough. If an impermeable

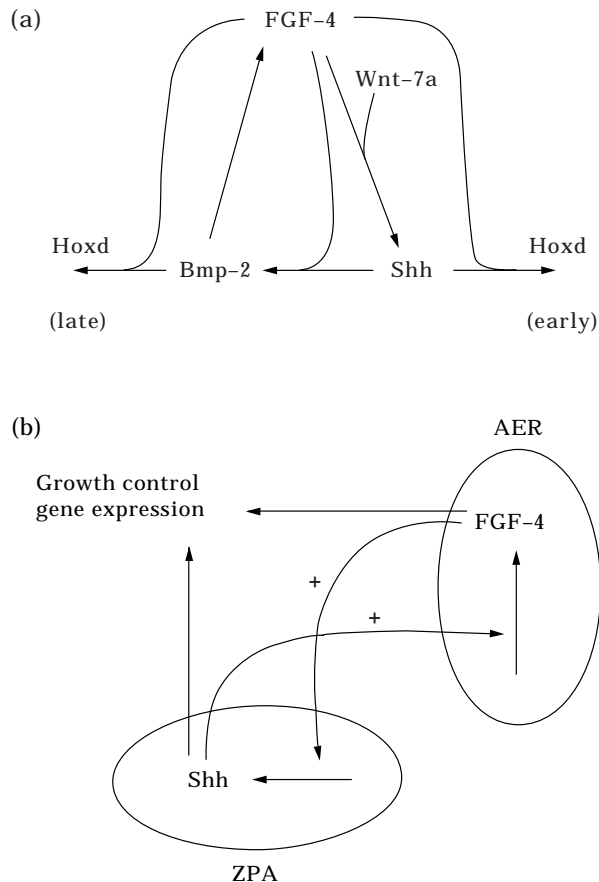


FIG. 3. (a) A model for the interactions of the three major putative morphogens, FGF-4, Shh, and Bmp-2, as proposed by Tickle and co-workers (Duprez *et al.*, 1996); (b) a schematic of the reduced kinetic interactions between ZPA, where production of Shh is affected by FGF-4 which diffuses from the AER, and the reciprocal effect of Shh on production of FGF-4 in the AER.

barrier is placed along the PD axis, then skeletal development occurs only on the posterior side of the barrier, which suggests that a diffusible morphogen is produced at the ZPA (Summerbell, 1979). The gradient model predicts that transplants of ZPA at positions along the AP axis of a stage 16 wing bud should result in either the elimination of the humerus, or its duplication, or the formation of a mirror-image duplicate of a single humerus, depending on the position of the graft and on the threshold concentration. However, in no cases is the humerus eliminated and rarely is it duplicated. Usually either a normal or a mirror-image duplicate humerus forms (Wolpert, 1987). The theory also predicts that multiple ZPA grafts should lead to fused or abnormally thick

digits, contrary to observation. Wolpert and Hornbruch (Wolpert, 1987) conclude from this that there is another mechanism at work which controls the thickness of the digits.

The progress zone model, in which differentiation is controlled by the number of divisions a cell undergoes while in the progress zone, was proposed to explain pattern formation and differentiation in the PD direction (Wolpert *et al.*, 1975). It predicts that removal of the AER will lead to distal truncation, as is observed, and it makes other predictions on the outcome of grafting a donor wing tip onto a host stump which agree closely with observation (Summerbell & Lewis, 1975). However, it does not have any regulative properties and thus cannot account for the immense capability of the early limb bud to regulate. For instance, removal of slices of the early limb bud perpendicular to the PD axis can lead to normal limbs (Summerbell, 1977), but according to the model, this should produce deletions along the PD axis of the final pattern. Oster *et al.* (1983) proposed a different model for pattern formation, one in which condensation of cells produces the patterning. However, it has recently been shown that if two anterior stage 20 limb halves are combined, the recombinant frequently forms two humeral elements (Wolpert & Hornbruch, 1990). This suggests that the anterior half of the limb contains cells that are already determined at this stage, yet visible aggregation of cells does not occur until much later (Wolpert & Hornbruch, 1990). Several other models, including some based on formal rules of growth and patterning (Wilby & Ede, 1975), and others based on the reaction and diffusion of morphogens (Meinhardt, 1982), have been proposed. Wilby & Ede (1975) show that formal rules for cell growth, division and movement can reproduce the shape of the growing limb bud, but their model has no morphogens. Meinhardt (1982, 1983) studies reaction–diffusion models of activator–inhibitor type for patterning along the AP and DV axes and shows how secondary fields can be generated by the interaction of the primary patterns. However these models involve autocatalytic production of the morphogens throughout the growing tissue, and there is no interaction between the ZPA and the AER

morphogens in determining the positional information along the AP axis. As we indicated earlier, the preponderance of current experimental information suggests that the primary morphogens are produced in specialized regions on the boundary of the limb bud, and that the two regions are coupled by diffusion of morphogens between them.

#### 1.4. OUTLINE OF A MODEL FOR GROWTH AND PATTERN FORMATION IN THE LIMB

Thus there is currently no model that can successfully explain the experimental observations, and we believe that there are several reasons for this. Firstly, existing models assume that patterning occurs separately in the AP and PD directions, but transplant results show a dependence on the distance between the ZPA and the AER (Wolpert, 1987), and on the position along the PD axis at which the graft is implanted in the host (Javois & Iten, 1981). Evidence cited previously gives the biochemical basis of the interaction between the AER and the ZPA. Secondly, none of the existing models incorporate interactions between morphogens and growth, and thus none can adequately represent the effect of growth on the spatio-temporal patterns of the morphogens. Finally, none account for the role of the non-AER ectoderm in patterning, nor do they incorporate any control of cell–cell communication in the patterning process. As we stated earlier, our long-term aim is to develop a model that will enable us to test various hypotheses concerning pattern formation in the limb, and to develop a computational model useful for understanding growth and patterning in other contexts. A minimal limb model involves at least two space dimensions, boundary conditions that vary with position on the boundary, and a domain of variable shape. To assist readers in understanding the biological basis of the model, without necessarily understanding the mathematical implementation of it, we first give a detailed verbal description of the model.

In the model we treat the growing limb as a two-dimensional region which begins as a truncated disk, but whose shape is determined by the forces exerted by the growing tissue. This can be thought of as a section through the limb taken

at the centerline in the DV direction. Although this precludes analysing transplants in which the DV polarity is altered (Javois & Iten, 1986), it is an essential first step, given the complexity of the system. It is essential that growth be included in a model, for the length increases from  $\sim 0.25$  to  $\sim 1.75$  mm in the 36 hours between stage 18 and stage 25, and patterning occurs in this interval\*. Differential or localized growth such as occurs after a ZPA transplant (Summerbell, 1981), is included in the model.

The model involves two diffusible morphogens that are produced in specialized regions near the periphery of the limb and diffuse throughout the interior of it. The AER is modeled as a distinct region on the distal boundary that serves both as the source of a substance that maintains cells in the undifferentiated state and as the source of one of the morphogens. The first assumption will be that the maintenance factor and the morphogen are identical, but that can be modified in later versions.

We model the AER as a specialized region at the distal end of the limb that serves as a morphogen source, the strength of which depends on the ZPA factor. The size of the AER, and hence the total amount of morphogen released, can be dynamically adjusted to conform with the observed changes of its size from stage 17 onward. The existing one-dimensional models assume that the concen-

tration, rather than the flux, is specified at the boundary. However, our assumption seems more appropriate because a constant concentration requires a mechanism by which the concentration is sensed and the production and/or release rates adjusted to maintain the concentration constant. In contrast, we simply prescribe a certain capacity for producing the morphogen in the AER region.

The ZPA is the source of the second morphogen. It is located on the posterior boundary near the distal end of the limb, and as with the AER, we assume that it has a given capacity to produce the morphogen. It is known that the ZPA originates at the flank but moves distally as the limb grows, and we incorporate this in the model by specifying that the ZPA remain within a fixed distance of the AER. Also, the ZPA is restricted to interior tissue near the boundary. All ectoderm is assumed to be impermeable to both morphogens, and both morphogens are degraded in the interior of the region. Initially we will assume that the concentration of the morphogens satisfies a zero flux condition at the proximal boundary, where the limb attaches to the flank *in vivo*, but other types of boundary conditions will be tested in later work†.

There are numerous questions that can be studied through use of the computational model, including the following.

- What is the spatial distribution of the morphogens, assuming that they are only produced in a zone near the boundary, and how does their distribution depend on parameters such as the production rates and diffusion coefficients? Can this distribution be established in the available time for reasonable values of the diffusion coefficients, both under normal conditions and after transplants of the ZPA? Does the spatio-temporal history of cells correspond with results obtained from fate maps?
- Can one define a threshold-based combinatorial scheme of interpretation of the instantaneous concentration landscape or the history of the landscape that will lead to the observed spatial pattern of gene expression? The existence of two spatially-separated

\* If we assume that the diffusion coefficient  $D$  is  $1 \times 10^{-7} \text{ cm}^2 \text{ s}^{-1}$ , then the characteristic time  $\tau \equiv L^2/2D = \sim 55$  hours for a length of 2 mm. Thus in the later stages of patterning the characteristic diffusion time-scale is certainly comparable to the time-scale for growth. If even the diffusion coefficient is 10 times this value the statement still holds true.

† Specifying a zero concentration at the proximal boundary rather than a zero flux has a substantial conceptual attraction in that the concentration of the morphogen produced at the AER would rise in the progress zone as the limb elongates. In other words, labile cells that leave the progress zone in the early stages of outgrowth experience a lower concentration of this morphogen than do those that emerge later. In view of this, a sequence of thresholds could produce the partitioning in the PD direction into three levels that could correspond to humerus, radius and ulna, and wrist and digits. This hypothesis is consistent with the observations that exchange of the AER does not change the fate of the underlying tissue, for we would interpret this as just a replacement of one source with another.

sources of the morphogens and the two-dimensionality of the underlying spatial domain make it plausible that such an interpretation function can be devised.

- Can the model explain a significant fraction of transplant results that are not explicable by the existing one-dimensional models? In particular, can one explain the effect of the distance between the transplanted ZPA and the existing AER, particularly for those transplants that produce splitting of the bud? Can one explain why removal of a rectangle of tissue without rejoining the cut edges leads to a partial loss of skeletal elements, whereas when the boundaries are sewn together, a normal wing results (Javois & Iten, 1981)? Similarly, does the model exhibit the degree of regulation observed following other types of surgical intervention, and what is the role of cell–cell communication and growth in this regulation?
- Is it necessary to include some level of self-organization in the model to account for the fact that mesodermal cells that are separated and allowed to reaggregate in an ectodermal jacket without a ZPA form moderately good digits (Pautou, 1973)? The experimental results on this point are not clear-cut, for the effect may be due to sorting of cells that are already differentiated, in which case the experiment has no bearing on pattern formation.

The first two will be addressed here; the others will be studied in future publications.

The model presented in this paper consists of a fluid-mechanical component that describes limb bud outgrowth, a reaction–diffusion–advection component that determines the spatio-temporal distribution of the morphogens, and a moving boundary that represents the mechanical and biochemical properties of the limb bud ectoderm. We do not incorporate any augmentation of cell movement in response to the local environment, for example due to chemotaxis, but this can be incorporated in the future if the results indicate the need for it. In the following section we describe the mathematical formulation of the model and in Section 3 we present some analytical results for simplified geometries and kinetics. In Section 4 we present numerous

simulations designed to illustrate the predictions made by the model. This section can be read independently of the preceding two by readers who wish to skip the mathematical details.

## 2. Mathematical Formulation of the Model for a Growing Limb

The first step will be to develop the fluid-mechanical description for the growth and movement of tissue in the limb. This component of the model requires detailed elaboration, because to our knowledge, this type of description has not been used before. We model the tissue as a viscous, incompressible fluid whose volume increases by virtue of a distributed source that stems from cell division and growth. The boundary of the limb is regarded as an elastic medium, and outgrowth results from the “pressure” of the increasing volume against this boundary. The processes involved are depicted in the schematic shown in Fig. 4. The equations for the fluid motion that drives outgrowth are given in the following subsection. The reaction–diffusion equations that govern the evolution of the morphogen distributions in space and time are given in Subsection 2.2, and a scaled version of the complete set of governing equations is given in Subsection 2.3.

### 2.1. TISSUE GROWTH AND MOVEMENT

The tissue in a growing limb is a complex mixture of cells, extracellular matrix, and other

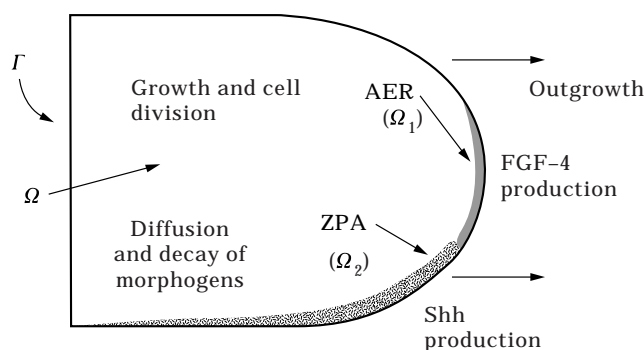


FIG. 4. A schematic of the growing limb and the processes involved in the limb. The interior of the limb is denoted  $\Omega$ , the AER region is denoted  $\Omega_1$ , the ZPA region is denoted  $\Omega_2$ , and the boundary of the limb is denoted  $\Gamma$ .

components, and to our knowledge its rheological properties have not been investigated. However the mechanical properties of other embryonic chick cell aggregates have been studied by Philips & Steinberg (1969), Philips *et al.* (1977) and Philips & Steinberg (1978). In a long-term culture vertebrate tissue masses exhibit liquid-like characteristics in response to stress, but the short-term response is more like that of an elastic solid. Philips *et al.* (1977) describe this tissue as an “elasticoviscous” liquid, but a more common terminology is to describe it as a viscoelastic material (Fung, 1993). Since we are only interested in the slow motion due to growth we neglect the elastic component of the response and model the tissue as a viscous fluid. The process of cell growth and cell division requires transport of nutrients via diffusion and convection across the limb bud ectoderm and through the extracellular matrix, and at a later stage, through the capillary system. We idealize this complex process as a distributed source  $S(\mathbf{c}, \mathbf{x}, t)$  of volume within the limb bud\*. The local source strength may depend upon chemical species such as growth factors contained in  $\mathbf{c}$ , the location  $\mathbf{x}$  of the tissue within the limb bud, and the age of the limb.

We assume that the fluid density is constant, but since there is growth, the continuity equation takes the form

$$\nabla \cdot \mathbf{u} = S(\mathbf{c}, \mathbf{x}, t). \quad (1)$$

wherein  $\mathbf{u}$  is the local fluid velocity. Later we will indicate how this growth term depends on the morphogen concentrations and other variables. We further assume that the fluid motion is described by the Navier–Stokes equations, which provide the simplest description of a viscous fluid. These are given by (Batchelor, 1973)

$$\begin{aligned} \rho \frac{\partial \mathbf{u}}{\partial t} + \rho(\mathbf{u} \cdot \nabla)\mathbf{u} = -\nabla p \\ + \mu \left( \nabla^2 \mathbf{u} + \frac{1}{3} \nabla S \right) + \rho \mathbf{F}. \end{aligned} \quad (2)$$

\*  $S$  is the volumetric growth per unit volume per unit time.

Here  $\rho$  is the fluid density,  $p$  is the pressure, and  $\mu$  is the fluid viscosity. The term  $\mathbf{F}$  is the force density (force per unit area in two dimensions) that limb bud ectoderm exerts on the fluid surrounding it. As will be seen below,  $\mathbf{F}$  is non-vanishing only in thin layers surrounding the limb bud boundary.

Equations (1) and (2) describe the tissue dynamics in the interior of the limb. In addition, the growth model must include a moving boundary  $\Gamma$  that represents the limb bud boundary. The instantaneous configuration of the boundary in two dimensions is given by the function  $\mathbf{X}(s, t)$ , where  $s$  is a Lagrangian label for a point on the boundary. We specify that  $\mathbf{X}(s, t)$  moves at the local fluid velocity, and therefore

$$\frac{\partial \mathbf{X}}{\partial t} = \mathbf{u}(\mathbf{X}(s, t), t). \quad (3)$$

Since the limb boundary is treated as an elastic material, the force per unit length  $\mathbf{f}(s, t)$  at each point on the boundary is a function of the instantaneous configuration. In a three-dimensional model the limb bud boundary could be modeled entirely by tangential elastic spring forces. In two dimensions, we include elastic links between the anterior and posterior edges to represent the circumferential forces in the three-dimensional ectoderm that prevent the limb bud from ballooning outward. The boundary is taken to be neutrally buoyant and thus the limb bud boundary forces are transmitted directly to the fluid via the force density  $F$ , which is given by

$$\mathbf{F}(\mathbf{x}, t) = \int_{\Gamma} \mathbf{f}(s, t) \delta(\mathbf{x} - \mathbf{X}(s, t)) ds. \quad (4)$$

In this equation the integration is over the points of the boundary  $\Gamma$  and  $\delta$  is the two-dimensional Dirac delta function. The limb bud grows out from the flank of the embryo, and for simplicity we regard the flank as an immovable boundary. This is accomplished by tethering the points on the proximal boundary in Fig. 4 to fixed points in space with stiff elastic spring forces.

## 2.2. THE REACTION–DIFFUSION–CONVECTION EQUATIONS FOR THE MORPHOGENS

In the interior  $\Omega$  of the limb the evolution of the morphogens  $\mathbf{c} = (c_1, c_2)$ , where  $c_1$  represents the AER morphogen and  $c_2$  represents the ZPA morphogen, is described by a system of reaction–diffusion–convection equations of the following form.

$$\frac{\partial \mathbf{c}}{\partial t} + \nabla \cdot (\mathbf{u}\mathbf{c}) = D\nabla^2 \mathbf{c} + \mathbf{R}(\mathbf{c}) \quad (5)$$

The diffusion matrix  $D$  is a diagonal matrix whose entries are the diffusion coefficients of the two morphogens. We have assumed here that the diffusion coefficients are constants, but we could easily incorporate dependence on the morphogens to describe control of cell–cell communication by the morphogens.

As we indicated previously, the AER morphogen is only produced in the AER ( $\Omega_1$ ) and the ZPA morphogen is only produced in the ZPA ( $\Omega_2$ ). Thus  $\mathbf{R} = (R_1, R_2)$  has the form

$$R_k = \begin{cases} r_k(\mathbf{c}) - \kappa_k c_k & \mathbf{x} \in \Omega_k \\ -\kappa_k c_k & \text{otherwise,} \end{cases} \quad (6)$$

where  $r_k(\mathbf{c}) > 0$  except possibly at  $\mathbf{c} = \mathbf{0}$ .

The convective term  $\nabla \cdot (\mathbf{u}\mathbf{c})$  in eqn (5) can be written as  $c\nabla \cdot \mathbf{u} + \mathbf{u} \cdot \nabla c$ , and using the growth as given by eqn (1), eqn (5) becomes

$$\frac{\partial \mathbf{c}}{\partial t} + S\mathbf{c} + \mathbf{u} \cdot \nabla \mathbf{c} = D\nabla^2 \mathbf{c} + \mathbf{R}(\mathbf{c}). \quad (7)$$

On  $\Gamma$  we specify the homogeneous Neumann or no-flux boundary conditions

$$\mathbf{n} \cdot D\nabla \mathbf{c} = 0, \quad (8)$$

where  $\mathbf{n}$  is the outward normal to  $\Gamma$ .

## 2.3. SCALING OF THE EQUATIONS

In order to cast the governing equations into dimensionless form, we introduce characteristic length and velocity scales and a characteristic chemical concentration, which we denote by  $L$ ,  $U$  and  $C$ , respectively. We then define the following scaled variables:  $\tau = t/T$ ,  $\bar{\mathbf{x}} = \mathbf{x}/L$ ,  $\bar{\mathbf{X}} = \mathbf{X}/L$ ,  $\bar{\mathbf{u}} = \mathbf{u}/U$ ,  $\bar{c} = c/C$  and  $\bar{p} = p/P$ ,  $\bar{S} = S/S_0$ . We further set  $T = L/U$ ,  $P = \rho U^2$  and

$S_0 = 1/T$ , and then obtain the following dimensionless equations.

$$\frac{\partial \bar{\mathbf{u}}}{\partial \tau} + (\bar{\mathbf{u}} \cdot \nabla) \bar{\mathbf{u}} = -\nabla \bar{p} + \text{Re}^{-1} \left( \nabla^2 \bar{\mathbf{u}} + \frac{1}{3} \nabla \bar{S} \right) + \bar{\mathbf{F}}$$

$$\frac{\partial \bar{\mathbf{c}}}{\partial \tau} + \bar{S} \bar{\mathbf{c}} + \bar{\mathbf{u}} \cdot \nabla \bar{\mathbf{c}} = \bar{D} \nabla^2 \bar{\mathbf{c}} + \bar{\mathbf{G}}(\bar{\mathbf{c}})$$

$$\frac{\partial \bar{\mathbf{X}}}{\partial \tau} = \bar{\mathbf{u}}(\bar{\mathbf{X}}(\sigma, \tau), \tau)$$

$$\nabla \cdot \bar{\mathbf{u}} = \bar{S}(\bar{\mathbf{c}})$$

$$\bar{\mathbf{F}}(\bar{\mathbf{x}}, \tau) = \int \bar{\mathbf{f}}(\sigma, \tau) \delta(\bar{\mathbf{x}} - \bar{\mathbf{X}}(\sigma, \tau)) d\sigma. \quad (9)$$

Here the Reynolds number  $\text{Re}$  is defined as  $\text{Re} = LU/\nu$ , where  $\nu = \mu/\rho$  is the kinematic viscosity. The remaining quantities are defined as  $\bar{\mathbf{F}} = L\mathbf{F}/U^2$ ,  $\bar{\mathbf{f}} = L\mathbf{f}/U^2$ ,  $\bar{\mathbf{G}} = L\mathbf{R}/(CU)$ ,  $\bar{S} = LS/U$ ,  $\bar{D} = D/(LU)$ ,  $\sigma = s/L$ . To simplify the notation the overbars are dropped hereafter, but all variables remain dimensionless.

A characteristic length-scale for vertebrate limb development is  $L = 0.1$  cm, the approximate width of the early chick limb bud. Between stages 18 and 25 the PD length of the wing bud increases from approximately 0.023 to 0.174 cm over a time span of approximately 36 hours. Thus the average rate of limb bud outgrowth is approximately  $0.0042$  cm hr<sup>-1</sup>, which yields a characteristic velocity  $U = 1.2 \times 10^{-6}$  cm s<sup>-1</sup>. For these characteristic length- and velocity-scales, a unit of dimensionless time  $\tau$  corresponds to approximately 23.15 hr. The Reynolds number for these values of  $U$  and  $L$  for a fluid with a kinematic viscosity of water ( $\nu \approx 0.01$  cm<sup>2</sup> s<sup>-1</sup>) is  $\text{Re} \sim 10^{-5}$ . Since reasonable values of  $\nu$  for mesodermal tissue are likely to be several orders of magnitude larger,  $\text{Re}$  may be several orders of magnitude smaller. Initially, we shall take the diffusion rate for growth factors in limb tissue to be approximately  $10^{-7}$  cm<sup>2</sup> s<sup>-1</sup>. This gives us a dimensionless diffusion coefficient  $D \approx 1$ .

## 2.4. NUMERICAL SOLUTION OF THE MODEL SYSTEM

The numerical algorithm for solving the complete model equations given by the system at (9) is based on the immersed boundary method, first used by Peskin (1977) to model blood flow

in the heart. This method has since been developed into a general method that can be used to study flows interacting with moving elastic structures. Details of the implementation of the numerical algorithm are described in the Appendix. A crucial feature of this method in our application is that the limb bud is not the entire computational domain for the solution of the fluid dynamical equations. The limb is embedded within a larger rectangular domain and within this larger domain, the limb bud boundary contributes a singular force field in the fluid equations. The volumetric sources that model growth in the limb are balanced by sinks distributed in the region exterior to the limb. Because the fluid equations are solved on a fixed regular domain, we can impose periodic boundary conditions and can solve the discretized Navier–Stokes equations using a Fast Fourier Transform algorithm. The advection–diffusion–reaction equations for the morphogens are solved using a finite difference method with an upwind scheme for the advection. The method for approximating the Neumann boundary conditions for the morphogens at the moving limb bud boundary [eqn (8)] is discussed in the Appendix.

### 3. Simplified One-dimensional Models

#### 3.1. SPATIALLY-LOCALIZED AER AND ZPA

To gain some insight into the effect the spatial separation between the AER and the ZPA has on the magnitude and spatial distribution of the morphogen concentrations, we consider several one-dimensional model problems in which the growth, and hence the fluid velocity, is zero. The first problem, which will show the effect of diffusion coefficients and decay constants on the distributions that result from coupled, spatially-separated, positive feedback mechanisms, is one in which the enzymes are localized at opposite ends of an interval. Thus the terms  $r_i$  in (6) are localized in space, but the degradation of the morphogens occurs throughout the domain. Since the equations have been non-dimensionalized, the interval is  $[0, 1]$ , and we suppose that the AER is at  $x = 1$  and the ZPA at  $x = 0$ . In this situation the governing equations for the morphogen concentrations reduce to

$$\begin{aligned} \frac{\partial c_1}{\partial t} &= D_1 \frac{\partial^2 c_1}{\partial x^2} - \kappa_1 c_1 \\ \frac{\partial c_2}{\partial t} &= D_2 \frac{\partial^2 c_2}{\partial x^2} - \kappa_2 c_2 \end{aligned} \quad (10)$$

for  $x \in (0, 1)$ , with the boundary conditions

$$-D_2 \frac{\partial c_2}{\partial x}(0, t) = r_2(c_1(0, t)) \quad (11)$$

$$D_1 \frac{\partial c_1}{\partial x}(1, t) = r_1(c_2(1, t)) \quad (12)$$

$$-D_1 \frac{\partial c_1}{\partial x}(0, t) = D_2 \frac{\partial c_2}{\partial x}(1, t) = 0. \quad (13)$$

These equations reflect the assumptions that the morphogens diffuse throughout the domain and are degraded by first-order reactions, that the production of ZPA morphogen at  $x = 0$  is controlled by the amount of AER morphogen present, and that the production of AER morphogen at  $x = 1$  is controlled by the amount of ZPA morphogen present at  $x = 1$ . It should be noted that each morphogen only *controls* the production rate of the other; it is itself not consumed in the process.

We first show how to obtain time-independent solutions of these equations, which must satisfy the system

$$D_1 \frac{d^2 c_1}{dx^2} - \kappa_1 c_1 = 0 \quad (14)$$

$$D_2 \frac{d^2 c_2}{dx^2} - \kappa_2 c_2 = 0 \quad (15)$$

$$-D_2 \frac{dc_2}{dx}(0) = r_2(c_1(0)) \quad (16)$$

$$D_1 \frac{dc_1}{dx}(1) = r_1(c_2(1)) \quad (17)$$

$$D_1 \frac{dc_1}{dx}(0) = D_2 \frac{dc_2}{dx}(1) = 0. \quad (18)$$

The solution of eqns (14) and (15) which satisfies the boundary conditions in eqn (18) is given by

$$c_1(x) = A_1 \cosh \sqrt{\frac{\kappa_1}{D_1}} x \quad (19)$$

$$c_2(x) = A_2 \cosh \sqrt{\frac{\kappa_2}{D_2}} (1 - x).$$

The amplitudes  $A_1$  and  $A_2$ , which must be positive, are determined from the remaining boundary conditions given in eqns (16) and (17). Thus the AER morphogen  $c_1$  has a maximum at  $x = 1$ , and the ZPA morphogen has a maximum at  $x = 0$ , as expected. One finds that the amplitudes of these distributions are solutions of the nonlinear system

$$D_2 A_2 \sqrt{\frac{\kappa_2}{D_2}} \sinh \sqrt{\frac{\kappa_2}{D_2}} = r_2(A_1) \tag{20}$$

$$D_1 A_1 \sqrt{\frac{\kappa_1}{D_1}} \sinh \sqrt{\frac{\kappa_1}{D_1}} = r_1(A_2).$$

We assume that  $r_1(0) = r_2(0) = 0$ , which simply means that there is no basal production of morphogen in the absence of the other morphogen. This could easily be changed without altering the overall conclusion significantly. Under this assumption the system (20) always has the solution  $(A_1, A_2) = (0, 0)$  for all values of the  $D_i$ s and  $\kappa_i$ s but the question is whether it has a non-zero solution. One sees from (20) that if one of the  $A_i$ s is zero then so is the other, so there is no possibility of a non-zero concentration of one morphogen and a zero concentration of the other.

We can write (20) in the form

$$A_2 = \Omega_2 \cdot r_2(A_1) \tag{21}$$

$$A_1 = \Omega_1 \cdot r_1(A_2) \tag{22}$$

where

$$\Omega_i^{-1} \equiv \sqrt{\kappa_i D_i} \sinh \sqrt{\frac{\kappa_i}{D_i}},$$

and then there is a positive solution for  $A_1$  and  $A_2$  if and only if the curves defined by (21) and (22) intersect in the interior of the positive quadrant of the  $A_1 - A_2$  plane. The rate functions  $r_i$  are typically monotone increasing functions, at least for small  $c$ , and they should saturate at large  $c$ . Under these two conditions one can show that there is at least one positive intersection of the curves if

$$\Omega_2 \left( \frac{dr_2}{dA_1} \right)_{(21)} > \frac{1}{\Omega_1} \left( \frac{dr_1}{dA_2} \right)_{(22)}^{-1},$$

when these are evaluated at  $(0, 0)$ . The subscripts (21) and (22) denote quantities computed from the equation with that number.

This cannot be determined in general without knowledge of the rate functions, and we therefore suppose that

$$r_1(c_2) = V_1 \frac{c_2}{K_2 + c_2} \quad r_2(c_1) = V_2 \frac{c_1}{K_1 + c_1}. \tag{23}$$

That is, we assume Michaelis–Menten kinetics for the production of both morphogens. We then have

$$A_2 = \Omega_2 V_2 \frac{A_1}{K_1 + A_1} \tag{24}$$

$$A_1 = \Omega_1 V_1 \frac{A_2}{K_2 + A_2}. \tag{25}$$

These can be solved explicitly and one finds that the non-zero solution is given by

$$A_2 = \frac{V_1 V_2 \Omega_1 \Omega_2 - K_1 K_2}{K_1 + V_2 \Omega_2} \tag{26}$$

$$A_1 = V_1 \Omega_1 \frac{A_2}{K_2 + A_2}. \tag{27}$$

Therefore  $(A_1, A_2) > (0, 0)$  if and only if

$$\frac{V_1 V_2}{K_1 K_2} > \Omega_1^{-1} \Omega_2^{-1}, \tag{28}$$

or

$$\frac{V_1}{K_2} \frac{V_2}{K_1} > \sqrt{\kappa_1 \kappa_2} \sqrt{D_1 D_2} \sinh \sqrt{\frac{\kappa_1}{D_1}} \sinh \sqrt{\frac{\kappa_2}{D_2}}. \tag{29}$$

On the left-hand side the term  $V_1/K_2$  (resp.  $V_2/K_1$ ) is the slope of the corresponding production term  $r_1$  (resp.  $r_2$ ) at zero concentration, while the right-hand side is determined by the diffusion coefficients and the decay rates.

If  $\kappa_i/D_i$  is small, either because the decay rates are small or the diffusion coefficients are large, then

$$\sinh \sqrt{\frac{\kappa_i}{D_i}} \sim \sqrt{\frac{\kappa_i}{D_i}}$$

and (29) reduces to

$$\frac{V_1 V_2}{K_2 K_1} > \kappa_1 \kappa_2. \tag{30}$$

This is purely kinetic criterion which simply states that the product of the maximal slopes of the production terms must exceed the product of the degradation rates.

At the other extreme, if the decay rates are too large there will certainly be no positive solution. Furthermore if all the kinetic parameters are fixed and the diffusion constants are decreased, then (29) will certainly not be satisfied for sufficiently small  $D_i$ s, and again there will be no positive solution. Since the length of the domain is used to make the diffusion coefficients dimensionless, one can always guarantee that there is no positive solution for sufficiently large  $L^*$ .

It is clear from the foregoing analysis that the condition

$$\frac{V_1 V_2}{K_2 K_1} - \sqrt{\kappa_1 \kappa_2} \sqrt{D_1 D_2} \sinh \sqrt{\frac{\kappa_1}{D_1}} \sinh \sqrt{\frac{\kappa_2}{D_1}} = 0 \tag{31}$$

represents a transverse bifurcation point at which a solution  $(A_1, A_2)$  passes from the third quadrant to the first quadrant as this quantity increases through 0. Further analysis shows that the positive solution for  $(A_1, A_2)$  is stable, at least when the difference in (31) is positive and sufficiently small.

### 3.2. DISTRIBUTED AER AND ZPA

The foregoing leads to an analytical criterion that guarantees a non-zero solution, and it indicates the interplay between production rates, decay rates, and the diffusion coefficients. However in reality both the AER and the ZPA are distributed over a region of the growing limb bud, and next we consider a one-dimensional

\* This has the interesting implication that the morphogenetic interactions between two spatially-separated organizing regions will be turned off when the size of the system reaches a critical value. This may be a useful mechanism in other contexts, such as in antero-posterior patterning in early development of the vertebrate neural plate, where signals from each end of a planar domain are thought to control patterning (Ruiz i Altaba, 1994).

model of this. We assume that the AER lies in the interval  $x \in (x_3, 1)$  and that the ZPA lies in the interval  $x \in (x_1, x_2)$ , where  $x_1 < x_2 \leq x_3 < 1$ . Thus we assume here that the ZPA occupies a fixed interval, but later we adopt a more functional definition of ZPA-ness.

In this case the reaction terms  $R_1$  and  $R_2$  in eqn (6) may be expressed in the form

$$\begin{aligned} R_1(x, \mathbf{c}) &= H(x - x_3)r_1(\mathbf{c}) - \kappa_1 c_1 \\ R_2(x, \mathbf{c}) &= H(x - x_1)H(x_2 - x)r_2(\mathbf{c}) - \kappa_2 c_2 \end{aligned} \tag{32}$$

where  $H$  is the Heaviside function ( $H(x) = 0$  for  $x \leq 0$  and  $H(x) = 1$  for  $x > 0$ ) and the  $r_i$  are as given in (23). The governing equations are

$$\begin{aligned} \frac{\partial c_1}{\partial t} &= D_1 \frac{\partial^2 c_1}{\partial x^2} + R_1(x, \mathbf{c}) \\ \frac{\partial c_2}{\partial t} &= D_2 \frac{\partial^2 c_2}{\partial x^2} + R_2(x, \mathbf{c}) \end{aligned} \tag{33}$$

for  $x \in (0, 1)$ , with the boundary conditions

$$D_1 \frac{\partial c_1}{\partial x}(0, t) = D_2 \frac{\partial c_2}{\partial x}(0, t) = 0 \tag{34}$$

$$D_1 \frac{\partial c_1}{\partial x}(1, t) = D_2 \frac{\partial c_2}{\partial x}(1, t) = 0. \tag{35}$$

In general one cannot obtain analytical solutions of these equations, but if both production rates are constant the equations are linear and uncoupled. This arises formally if both  $c_1$  and  $c_2$  are large relative to the corresponding Michaelis constant in the rate expressions, in which case the production rates are saturated, and we use this formal connection later. In this special case the steady-state distributions of the morphogens are given by the following equations

$$c_1(x) = \begin{cases} a_{10}(e^{\lambda_1 x} + e^{-\lambda_1 x}) & x \leq x_3 \\ a_{13}(e^{\lambda_1 x} + e^{\lambda_1(2-x)}) + \alpha_1 & x_3 < x \leq 1, \end{cases} \tag{36}$$

$$c_2(x) = \begin{cases} a_{20}(e^{\lambda_2 x} + e^{-\lambda_2 x}) & x \leq x_1 \\ a_{21}e^{\lambda_2 x} + b_{21}e^{-\lambda_2 x} + \alpha_2 & x_1 < x \leq x_2 \\ a_{22}(e^{\lambda_2 x} + e^{-\lambda_2(2-x)}) & x_2 < x \leq 1 \end{cases} \tag{37}$$

Here  $\alpha_i = V_i/\kappa_i$ ,  $\lambda_i = \sqrt{\kappa_i/D_i}$ ,  $i = 1, 2$  and the coefficients are given as follows.

$$\begin{aligned}
 a_{10} &= \alpha_1 \left( \frac{e^{\lambda_1 x_3} - e^{\lambda_1(2-x_3)}}{2 - 2e^{2\lambda_1}} \right), \\
 a_{13} &= \alpha_1 \left( \frac{e^{\lambda_1 x_3} - e^{\lambda_1(2-x_3)}}{2 - 2e^{2\lambda_1}} - \frac{e^{-\lambda_1 x_3}}{2} \right), \\
 a_{20} &= \alpha_2 \left( \frac{-e^{-\lambda_2(-2+x_2)} + e^{-\lambda_2(-2+x_1)} + e^{\lambda_2 x_2} - e^{\lambda_2 x_1}}{2e^{2\lambda_2} - 2} \right), \\
 a_{21} &= \alpha_2 \left( \frac{-e^{\lambda_2 x_1} + e^{\lambda_2 x_2} + e^{-\lambda_2 x_1} - e^{-\lambda_2(-2+x_2)}}{2e^{2\lambda_2} - 2} \right), \\
 a_{22} &= \alpha_2 \left( \frac{-e^{\lambda_2 x_1} - e^{-\lambda_2 x_2} + e^{\lambda_2 x_2} + e^{-\lambda_2 x_1}}{2e^{2\lambda_2} - 2} \right), \\
 b_{21} &= \\
 &\alpha_2 \left( \frac{-e^{\lambda_2(2+x_1)} - e^{-\lambda_2(-2+x_2)} + e^{-\lambda_2(-2+x_1)} + e^{\lambda_2 x_2}}{2e^{2\lambda_2} - 2} \right).
 \end{aligned} \tag{38}$$

In Fig. 5 we show the effect of changes in the diffusion coefficients of the species for fixed values of the kinetic parameters and the spatial domains in which the AER and ZPA are localized. In Fig. 5(a) we show a base case in which both diffusion coefficients are 1, and in the other panels we show the effect of varying the diffusion coefficients. Increasing  $D_i$  leads to flatter profiles, whereas decreasing  $D_i$  leads to

sharper profiles and higher concentration levels within the AER [Fig. 5(b)] and ZPA regions [Fig. 5(c)]. As  $D_i \rightarrow 0$  the solution approximates a step function with  $c_1 = V_1/\kappa_1$  in the AER and  $c_2 = V_2/\kappa_2$  in the ZPA.

### 3.3. THE INTERMEDIATE KINETIC REGIME

When the production rates are not constant one must resort to numerical computation of the solutions to eqns (33–35). Figure 6 shows the results for the kinetic parameters used in Fig. 5(a–c) and several values of the diffusion coefficients. One sees in Fig. 6(a) that at fixed  $D_2$ , increasing  $D_1$  (the diffusion coefficient of the AER morphogen) increases the level of the AER morphogen in the ZPA region and decreases it in the AER region. Because production of the ZPA morphogen depends on the level of the AER morphogen when the kinetics are not saturated, this leads to an increase in the level of the ZPA morphogen throughout the domain. Figure 6(b) shows that at fixed  $D_1$ , increasing  $D_2$  decreases the ZPA morphogen in the ZPA region and increases it elsewhere, thereby producing an increase of the AER morphogen. These results are qualitatively similar to what is shown in Fig. 5 because the kinetic terms are essentially saturated for the values of  $D_i$  shown, but here a change in either diffusion coefficient affects the distribution of both species. Furthermore, there is a significant difference between the results using constant production rates and concentration-dependent rates when both diffusion coefficients are very low. In the present case small diffusion rates (for example  $D_1 = 1$ ,

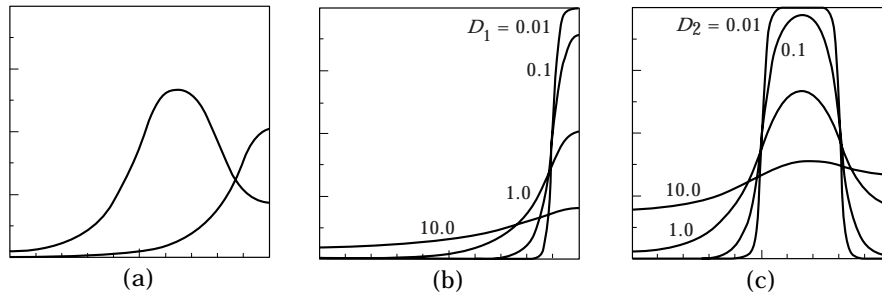


FIG. 5. Steady-state solutions with saturated kinetics.  $x_1 = 0.5$ ,  $x_2 = 0.8$ ,  $x_3 = 0.9$ .  $V_1 = V_2 = 2000$ ,  $\kappa_1 = 50$ ,  $\kappa_2 = 50$ . The horizontal axis is  $x \in [0, 1]$ , the vertical axis shows  $c_1$  and/or  $c_2 \in [0, 40]$  in dimensionless units. The values of the parameters  $V_k$  and  $\kappa_k$  are those used in the full simulations in a later section. (a)  $c_1$  (peak on right)  $c_2$  (central peak) with  $D_1 = 1$  and  $D_2 = 1$ ; (b)  $c_1$  with  $D_1 = 0.01, 0.1, 1, 10$ ; (c)  $c_2$  for  $D_2 = 0.01, 0.1, 1, 10$ . In (b) and (c) smaller diffusivities produce larger peak values in the morphogen concentration.

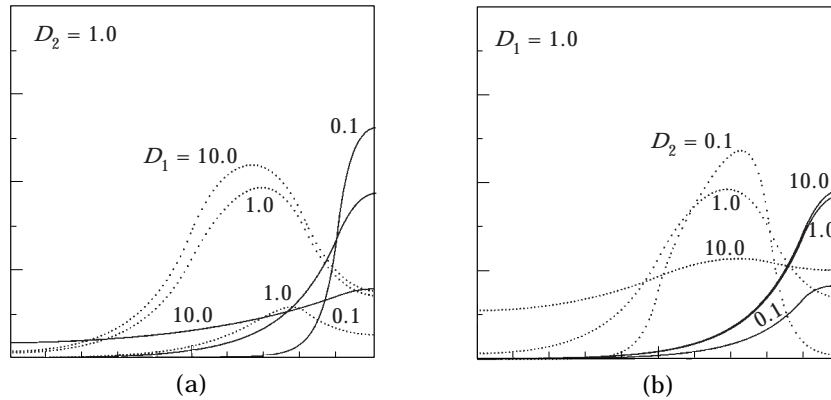


FIG. 6. Steady-state solutions to the evolution equations (33)–(35), computed using the same kinetic parameters and production regions as in Fig. 5. The horizontal axis is  $x \in [0, 1]$ , the vertical axis (range  $[0, 40]$ ) shows  $c_1$  (—) and  $c_2$  (· · ·) in dimensionless units. (a)  $D_2 = 1$  and variable  $D_1$ ; (b)  $D_1 = 1$  and variable  $D_2$ .

$D_2 = 0.01$ ) leads to solutions that converge to the steady state  $\mathbf{c} = (0, 0)$ , because there is insufficient transport of the complementary morphogen between the production sites to offset the degradation that occurs throughout the domain. By contrast, when production of a morphogen is independent of the level of the complementary morphogen, as in Fig. 5, the spatial distributions of the morphogens approach step functions supported on the production regions as the diffusion coefficients approach zero.

It is known that the maximum expression of ZPA activity is not immediately adjacent to the AER, but rather, lies in the region a few hundred microns proximal to the AER. The preceding results are consistent with this observation but they reflect the fact that the ZPA was specified geometrically rather than functionally. The mechanisms controlling the graded distribution of ZPA activity are not known at present, but one possibility is that it stems from spatially varying differences in the mesodermal tissue itself. An alternative is that the ZPA morphogen production exhibits a biphasic response to the AER morphogen. This could arise, for instance from activation of an enzyme at low AER morphogen levels and inhibition at high levels. Computations in which the production rate  $V_2$  depends on the concentration of the AER substance  $c_1$  as follows

$$V_2(c_1) = \begin{cases} 1.0 & \text{if } c_1 < c_1^s \\ 0 & \text{otherwise} \end{cases} \quad (39)$$

produce profiles of the ZPA substance that has a maximum at some distance from the AER, as in Fig. 6.

#### 4. Numerical Simulations Incorporating Growth and Cell Movement

##### 4.1. THE SPATIO-TEMPORAL DISTRIBUTIONS OF THE MORPHOGENS

In this section we describe numerical results from simulations of the full model, including growth and cell movement. Initially, the curved part of the limb bud boundary is an arc of a circle chosen to approximate a stage 19–20 limb bud. The initial configuration of the limb bud domain is the same in each of the four simulations described later.

The estimates of growth rates given earlier show that diffusion, and hence establishment of the morphogen distributions, is rapid compared with growth when the distances are small, but the time-scales of these processes become more comparable as outgrowth proceeds. To eliminate artifacts due to the initial morphogen distributions, we first set the growth to zero and compute an approximate steady state for the morphogen distributions. We then use this morphogen distribution as the initial condition for simulations that include growth and cell movement. The quasi-steady distributions for the morphogens are obtained by integrating the evolution eqn (5), with  $S \equiv 0$  and  $\mathbf{u} = 0$ , forward

in time, using the methods described in the Appendix, until the concentration distributions are approximately constant in time. Thus, the initial morphogen distributions are approximate solutions to the equation

$$D\nabla^2\mathbf{c} + \mathbf{R}(\mathbf{c}) = 0 \tag{40}$$

with boundary conditions given by eqn (8). Once the initial distributions for  $S = 0$  are determined, we turn on the growth rate throughout the limb. The dependence of the volumetric growth rate on the morphogens must be postulated, and we suppose that it depends only on  $c_1$ , the morphogen or growth factor produced in the AER, as follows.

$$S = s_1 c_1 + s_2. \tag{41}$$

The growth rate comprises a constant component  $s_2 = 0.1$  that represents a basal growth rate, and a component proportional to the concentration of the growth factor  $c_1$ . We set the first order rate constant  $s_1$  equal to  $10/3$ . An interpretation of (41) is that growth depends on binding of a growth factor to surface receptors, and that the concentration of growth factor is much less than the  $K_m$  for binding.

In the four simulations that follow the AER is a region in the limb bud of roughly constant dimensions localized along the distal edge of the limb bud. The ZPA-competent tissue is a region of constant width on the posterior edge of the limb bud, beginning at the proximal boundary and ending just short of the AER region. Although the width of ZPA-competent region is fixed, the ZPA-competent length elongates with limb bud outgrowth. The algorithms for determining the ZPA and AER regions are described in detail in the Appendix. As will be discussed below, the production rates of the AER and ZPA morphogens within these regions may vary both spatially and temporally. Since

\* We remark that the algorithm itself contains a slight asymmetry that arises as follows. A single boundary point is added whenever the boundary stretches by a prescribed amount. The new boundary point is inserted between the two adjacent immersed boundary points that have moved furthest apart. The addition of new points to the boundary generally does not occur symmetrically with respect to the PD axis.

the growth factor  $c_1$  is produced in the AER, the growth rates are highest in the distal region. This is consistent with experimental observations which show that the mitotic rate is highest in the PZ and about one-fourth that rate in the proximal limb bud.

*Simulation 1: Uncoupled AER and ZPA production.* As was discussed in the Introduction, the biochemical reactions that produce the AER and ZPA morphogens are believed to be coupled. However, to establish a base case for later comparison purposes we first suppose that the production rates of the morphogens are uncoupled. As a result, in this simulation active ZPA extends along the entire posterior margin of the domain. In later simulations, it is the interaction with the AER factor that limits the effective extent of the ZPA. Here the morphogen production rates  $R_k$  that appear in eqn (5) have the form

$$R_k(\mathbf{c}) = \begin{cases} \gamma_k(1 - c_k) & \mathbf{x} \in \Omega_k \\ -\kappa_k c_k & \text{otherwise} \end{cases} \tag{42}$$

for  $k = 1, 2$ . In all examples  $\Omega_1$  is identified with the AER and  $\Omega_2$  with the ZPA, as in Fig. 2. The dimensionless kinetic parameters are set at  $\gamma_k = 10000$  in this example in order to ensure that  $c_k$  will be approximately 1 in  $\Omega_k$ . The dimensionless diffusion constants are set at  $D_k = 1$  for  $k = 1, 2$  and the morphogen degradation rates are set at  $\kappa_k = 50$ . The outline of the growing limb bud domain and contours of the morphogen concentrations are shown at several time steps in Row I of Fig. 7. Since the production of  $c_1$  is independent of  $c_2$  and the AER is initially symmetric about the PD axis, the profiles of  $c_1$  are also symmetric about the PD axis initially, and because the local growth rates depend only on the concentration of  $c_1$ , limb bud outgrowth is also symmetric initially. One sees in the figure that the shapes of the limb bud and concentration profiles of the AER growth factor remain essentially symmetric about the PD axis throughout the entire period. The location of the immersed boundary points are obscured by the superposition of morphogen contours in this figure, but the reader can look at Fig. 8, to be described below, for a better picture of the boundary\*.

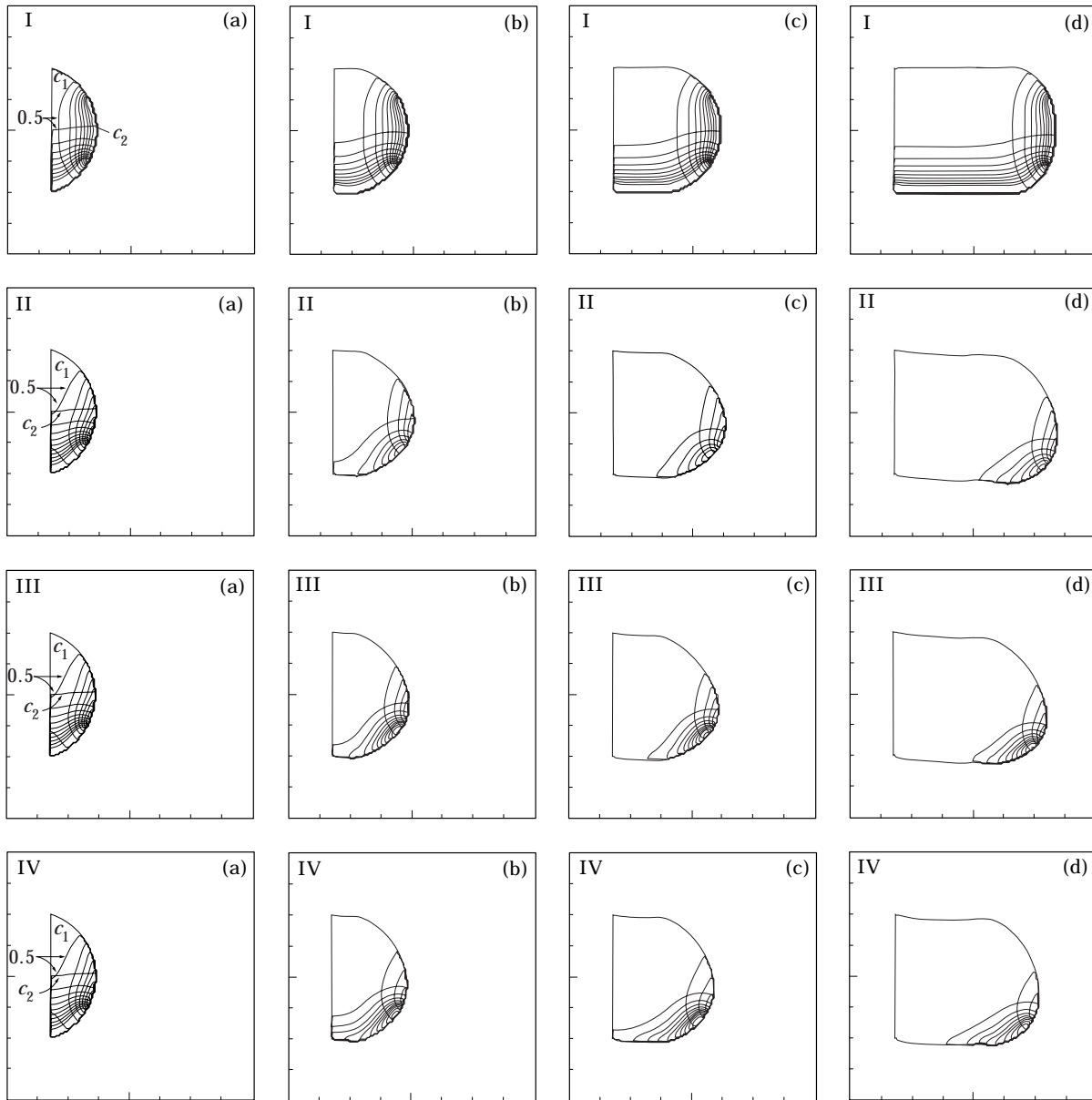


FIG. 7. Contour lines of the morphogen concentrations  $c_1$  and  $c_2$ . **Row I:** simulation 1 at dimensionless times (a) 0; (b) 0.5625; (c) 1.125; (d) 1.875 [real times of (a) 0; (b) 13; (c) 26; and (d) 43 hours]. **Rows II–IV:** simulations 2–4, showing the concentration contours at dimensionless times (a) 0; (b) 0.375; (c) 0.75; (d) 1.3125 [real times of (a) 0; (b) 8.7; (c) 17.4; (d) 30.4 hours]. If we identify panel (a) in each row with stage 19, then these times correspond to stages 19, 21, 23, and 25, respectively, in normal chick limb development. Here and hereafter, the bounding square in each panel delimits the computational domain, each side of which is 2.0 mm in length (see Appendix). The contours shown represent equally-spaced levels of  $c_1$ , which is highest near the AER and decreases monotonically along the PD axis, and  $c_2$ , which is highest along the posterior boundary and decreases monotonically along the posterior–anterior axis. In Row I the contour levels shown begin at 0.1 and increase in increments of 0.1 for each species. In Rows II–IV the contour levels begin at 0.5 and increase in increments of 0.5 for each species.

*Simulation 2: Coupled feedback interaction between AER and ZPA morphogen production.* In this simulation we use the Michaelis–Menten

kinetics given at (23) for the production of the morphogens and couple these with the standard linear decay terms. Thus the kinetic functions are

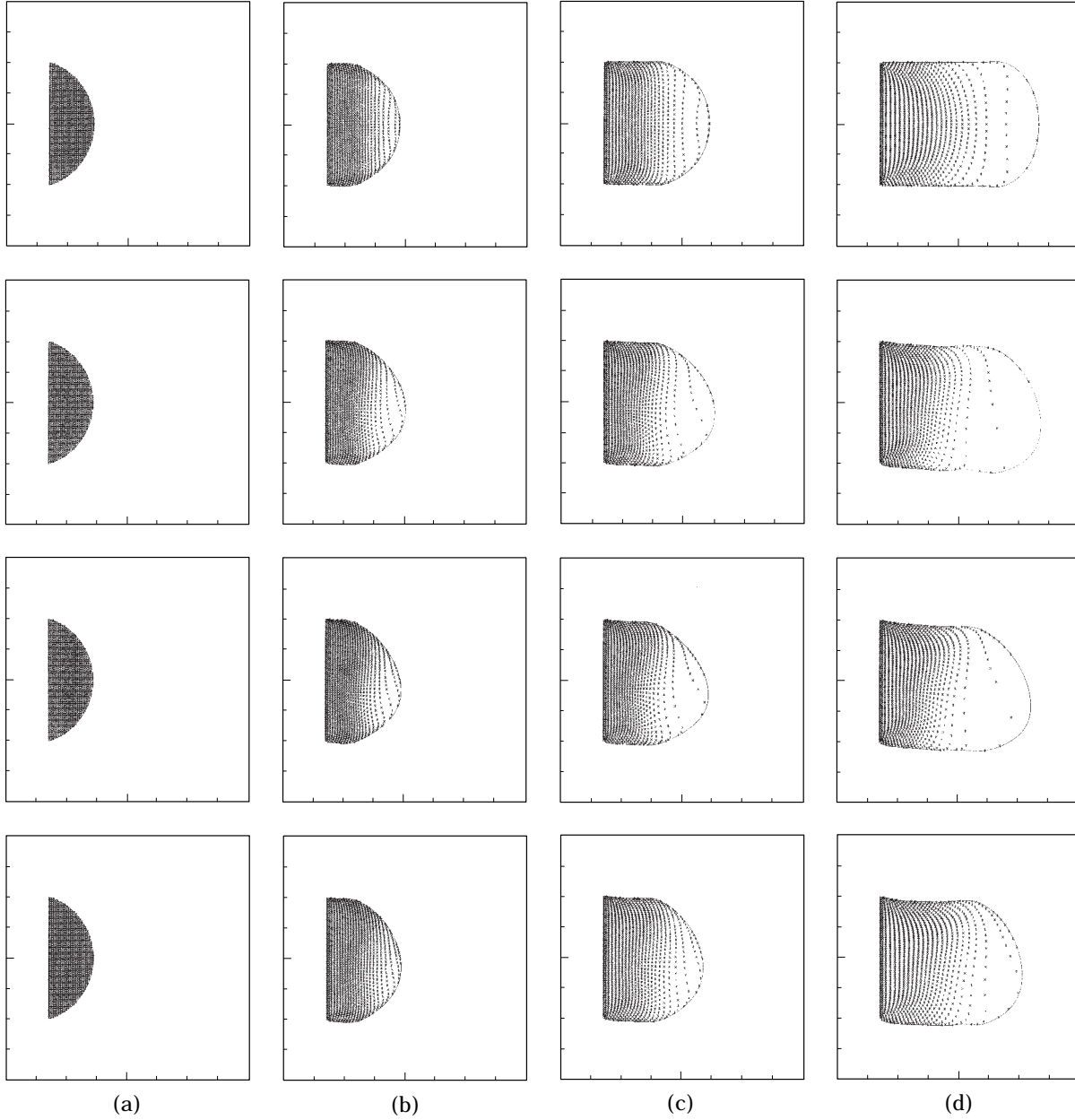


FIG. 8. The locations of fluid markers at selected times within the growing limb bud. The four rows correspond to the four rows shown in Fig. 7, and the time snapshots within a row correspond to those shown in that figure.

as follows.

$$\begin{aligned}
 R_1 &= V_1 \frac{c_2}{K_2 + c_2} - \kappa_1 c_1, \quad \text{for } \mathbf{x} \in \Omega_1 \\
 &\quad \text{and } R_1 = -\kappa_1 c_1, \quad \text{otherwise} \\
 R_2 &= V_2 \frac{c_1}{K_1 + c_1} - \kappa_2 c_2, \quad \text{for } \mathbf{x} \in \Omega_2 \\
 &\quad \text{and } R_2 = -\kappa_2 c_2, \quad \text{otherwise.} \quad (43)
 \end{aligned}$$

The dimensionless parameters are identical in both species and are set at  $V_k = 2000$ ,  $\kappa_k = 50$ ,  $K_k = 1$  and  $D_k = 1$ ,  $k = 1, 2$ . As in Simulation 1, the AER substance  $c_1$  is only produced in the AER, but it decays throughout the limb bud with time constant  $\kappa_1^{-1}$ . Similarly, the ZPA factor  $c_2$  is produced only in the ZPA and decays throughout the limb bud.

Row II in Fig. 7 shows the dramatic effect that spatial localization and coupling of the

production rates has on the spatio-temporal distributions of the morphogens. When compared with Row I, the high point of the AER morphogen distribution, which is slightly greater than 2 at the final time (panel II-d), shifts toward the ZPA and there is a gradient of AER factor within the AER, with  $c_1$  higher in the posterior and lower in the anterior portion of the AER. (Since the average level of  $c_1$  is higher in Row II than in Row I, the simulation in Row I was extended in time to produce the same overall growth.) The asymmetry in the production of the growth factor, which is higher in the posterior–distal region of the limb than in the anterior region, leads to a pronounced asymmetry in the shape of the growing limb. Note also that the maximum levels of both morphogens decrease as outgrowth proceeds, because both morphogens are degraded throughout the growing volume of tissue, but only produced in domains of constant size\*. For example the maximum of the ZPA factor exceeds 6 in panel a of Row II, whereas the maximum is only about 3.5 in panel d of that row.

*Simulation 3.* In this and the following simulation the reaction kinetics and kinetic parameters are identical to those in Simulation 2, but the diffusion coefficients are varied. In this simulation we set  $D_1 = 1$  and  $D_2 = 0.5$ , which means that the ZPA species diffuses at half the rate used in Simulation 2. One sees in Row III of Fig. 7 that the maximum concentration levels of  $c_2$  are higher at later times than in Simulation 2. In particular, the maximum value of  $c_2$  at the final time (panel d) is approximately 4.5 here, as compared with 3.5 at the same time in Row II. Furthermore, just as in the results for the one-dimensional simulations shown in Fig. 5, the concentration levels of  $c_2$  fall off more rapidly when the diffusion coefficient is reduced, and hence the contour levels are more compressed in space. Because the ZPA factor is more localized in space when its diffusion coefficient is reduced, this leads to a lower overall production of the growth factor and hence a reduction in the

outgrowth of the limb. Indeed, the final length shown in panel III-d is only 93% of the length at the same time shown in panel II-d. Since the only difference in the parameters between Row II and Row III is the change in the diffusion coefficient of the ZPA factor, this shows that the coupling between production of the factors can have unanticipated effects on the growth of the limb. We will say more about this phenomenon in the discussion of fluid markers below.

*Simulation 4.* In this simulation the diffusion coefficients are set at  $D_1 = 2$ ,  $D_2 = 0.5$ , and otherwise the parameters are the same as previously. The contours in  $c_1$  and  $c_2$  are shown in Row IV of Fig. 7. There are two significant effects of the increase in the diffusion of the AER factor. Firstly, the maximum levels of the AER factor are reduced significantly (the maximum of  $c_1$  is approximately 1.0 in panel d of Row IV, compared with just under 2.5 in panel d of Row II), because when the AER factor is more uniformly distributed in space the total degradation rate is increased substantially. As a result, the rate of limb bud outgrowth is lower in Simulation 4 than in Simulation 3. Secondly, the faster diffusion of the AER factor means the ZPA morphogen is produced in significant amounts over a larger portion of ZPA-competent tissue, and thus the concentration of the ZPA factor rises throughout much of the posterior margin of the limb. Thus the ZPA substance is more proximally expressed in Simulation 4 than in Simulation 3. However, the maximum concentration level of the ZPA species is lower in Simulation 4 (approximately 4) than in Simulation 3 (approximately 4.5).

#### 4.2. CELL TRAJECTORIES

Since growth in the limb is asymmetric when the ZPA and AER are localized in space and interact via diffusible substances, it is necessary to track cells in order to determine the temporal pattern of morphogen concentrations to which cells are exposed during outgrowth. Without this information it is difficult to propose mechanisms by which the morphogen concentrations can be translated into levels of gene expression. In addition to tracking the overall shape of the limb and the concentration distributions within it, we track individual fluid markers in each of the

\* The AER-competent region is of fixed size, but the ZPA-competent region elongates. Because of morphogen coupling, the active region of the ZPA species is localized distally and the size of the active region is roughly constant.

simulations described in the preceding section. These markers, which may be regarded as proxies for individual limb bud cells or their progeny, travel at the local fluid velocity, and thus accurately reflect the relative displacements between selected points in the limb as outgrowth proceeds.

Fluid markers are placed on each interior grid point at  $t = 0$ , and subsequently each marker is convected along at the local fluid velocity. The locations of these fluid markers within the growing domain for the four simulations described previously are shown in Fig. 8. Initially the markers are regularly spaced, since they coincide with the grid points, but because they move with the local velocity, which is determined by the local growth rate, the distance between adjacent pairs of markers changes with time. Evidence of high growth rates in the region of highest concentration of  $c_1$ , the AER growth factor, can be seen in the wider spacing of markers in the distal region, but there is a basal level of growth throughout the limb. The axially symmetric distribution of  $c_1$  in Simulation 1 (Row I Fig. 7) leads to axially symmetric growth rates and an axially symmetric fluid marker distribution (Row I of Fig. 8). The asymmetric distribution of  $c_1$  due to coupling with the ZPA morphogen  $c_2$  (see Rows II–IV of Fig. 7) results in asymmetric local growth rates and to a marked asymmetry in the fluid marker distribution, as shown in Rows II–IV of Fig. 8. In particular, the spacing between adjacent columns of fluid markers is much greater in the posterior–distal region than in the anterior–distal region. As noted above, the reduction of the diffusion coefficient  $D_2$  for the ZPA species in Simulation 3 results in a posterior shift in the production of the AER species. This change in the distribution of  $c_1$  results in more pronounced posterior–distal growth rates, as evidenced by the increased posterior spacing between adjacent columns of the distal fluid markers (cf. Row III

of Fig. 8). In Simulation 4 the diffusion constant  $D_2$  remains the same as in Simulation 3, but  $D_1$  is increased. This leads to a more uniform distribution of the AER factor  $c_1$  and more uniform growth throughout the limb, as can be seen in the fluid marker distribution shown in Row IV of Fig. 8.

Further insight into the pattern of cell movement during growth can be gained by plotting the trajectories of selected fluid markers. The results for the four simulations are shown in Fig. 9(a–d). Initially nine pairs of fluid markers, located along the posterior–distal edge of the limb bud are chosen from those shown in Fig. 8. The pairs are designated (a, A) . . . (i, I) from posterior to anterior. In each pair, the more proximal marker is designated by a lower-case letter, the distal marker by a capital letter. In panel 1 of Fig. 9 we show the tracks of the fluid markers for Simulation 1\*. The pair (e, E) is initially on the centerline in the PD direction and remains there throughout the simulation—a reflection of the axially-symmetric distribution of  $c_1$  and concomitant axially symmetric growth rates. The other pairs are displaced posteriorly or anteriorly, depending on their initial location. The trajectories for Simulation 2 are shown in panel 2 of Fig. 9, where it is seen that the pairs (d, D) and (e, E) are displaced anteriorly as well as distally. This anterior displacement results from higher growth rates in the posterior–distal region. As in Simulation 1, (a, A), (b, B), and (c, C) are displaced posteriorly and distally. The fact that growth occurs primarily near the AER is reflected in the fact that cell markers that initially lie near the AER are far removed from it at the final time.

Panel 3 of Fig. 9 shows the trajectories for Simulation 3, where, in contrast to Simulation 2, the fluid marker pair (c, C) follows a more axial path and (d, D) and (e, E) are displaced more anteriorly. As was noted in the previous section, the AER growth factor is more concentrated in the posterior–distal region of the limb bud in the third simulation. The higher growth rates in the posterior–distal region push the fluid marker pairs (c, C), (d, D), and (e, E) anteriorly. There is however less effect on the trajectories of cells that begin on the anterior side of the mid-line.

\* Since the computational domain is of fixed size and the fluid is incompressible, the volumetric source that arises from growth must be “absorbed” in sinks located outside the limb bud. These are placed at four grid points near the corners of the computational domain, and the results in Panel 1 show that the location of these sources preserves the symmetry of the results.

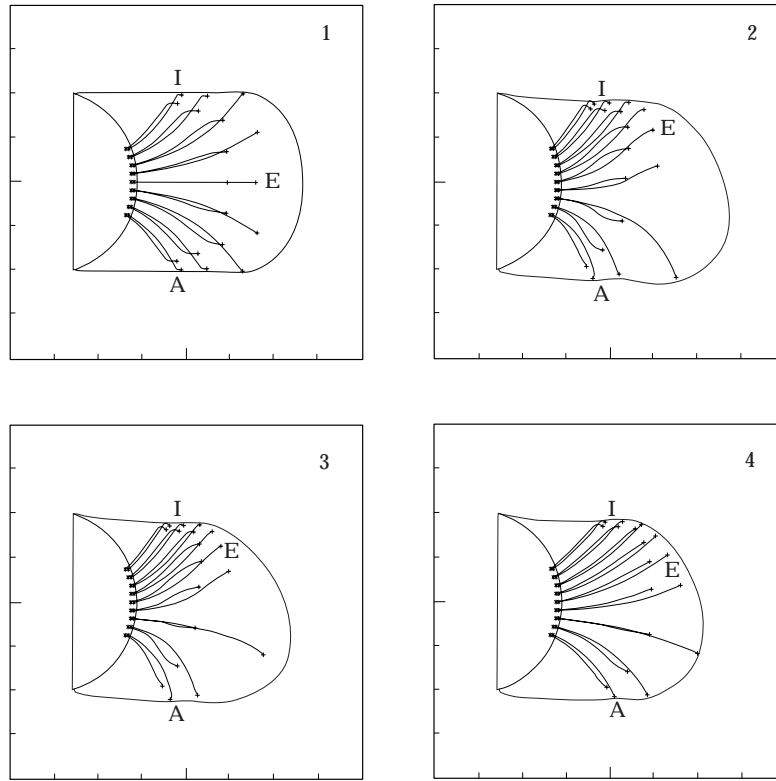


FIG. 9. Paths of selected fluid markers (a, A), . . . , (i, I) for simulations 1–4. Labels on the curves mark the trajectories of selected fluid markers.

The anterior displacement of these pairs is less pronounced in Simulation 4, as is shown in panel 4 of Fig. 9. This is consistent with the higher diffusivity of the AER factor, which leads to more uniform, albeit lower, growth rates throughout the limb bud (cf. also Rows III and IV of Fig. 8). In this simulation there is proportionately less growth near the AER, and cells that begin near the AER remain closer to it throughout outgrowth. An interpretation of this in the context of the progress-zone model described in the Introduction is that cells that begin in the progress zone never stray far from it; they are held more or less in their relative place by the growth that occurs proximally.

Since the trajectories of fluid markers can be interpreted as the trajectories of individual cells or their progeny, the preceding results show that the location of individual cells within the limb bud as a function of time depends on the details of the model, and in particular, is strongly

influenced by the diffusivities of the AER and ZPA factors. As can be anticipated and will be shown below, the time-dependent location of the cells relative to the AER and ZPA leads to a time-dependent micro-environment of morphogen levels to which the cells are exposed.

An alternate representation of the differential growth throughout the limb is obtained by following the motion of the trapezoidal blocks of tissue formed by connecting four adjacent markers, two in the proximal row and two in the distal row. The eight blocks that result are labeled as follows: Block 1: (a, A, b, B), Block 2: (b, B, c, C), . . . , Block 8: (h, H, i, I) (see Fig. 10). Each block undergoes growth, deformation and displacement during outgrowth, and the difference between the final and initial area of a block represents the cumulative growth in that block. The spatial location of a block at any time  $T$  can be interpreted as a fate map, from  $t = 0$  to  $t = T$ , for cells in that block. The details of this

transformation depend primarily on the local growth rate, which is governed by the spatio-temporal distribution of the morphogens. For example one sees that in Simulations 2–4, Block 3 is the largest and has a significant area in the post- and pre-axial regions. The boundary between Blocks 4 and 5 represents the midline at  $t = 0$ , and one sees that it suffers a substantial displacement in the anterior direction in Simulations 2–4.

4.3. MORPHOGEN CONCENTRATIONS ALONG CELL TRAJECTORIES

The local patterns of growth as a function of time, which are manifested in the separation between markers in Figs 8 and 9 and in the growth of area in Fig. 10, reflect the history of exposure to the growth-controlling morphogen at the fluid markers. On the other hand, the contour lines shown in Fig. 7 reflect an Eulerian or “fixed-in-space” viewpoint that reflects what a cell is exposed to at a certain point in space–time. At present it is not known whether

it is the instantaneous concentration of morphogens that determines gene activation, or whether it is the history of exposure (or at least a minimum exposure time) that is paramount. For this reason we next display the morphogen concentrations in the Lagrangian framework, in which concentrations are tracked along cell trajectories.

The morphogen concentration  $\tilde{c}_k(t)$  at the location of a fluid marker can be expressed as

$$\tilde{c}_k(t) = c_k(\mathbf{X}_i(t), t) \tag{44}$$

where  $\mathbf{X}_i(t)$  gives the path of the  $i$ -th marker. The concentrations  $\tilde{c}_k$  of the AER and ZPA substances at the location of the markers whose trajectories are given in Fig. 9 are shown as a function of time in Fig. 11. One sees there that in simulations 2 and 3 the concentration of the AER morphogen is a strictly decreasing function of time for all cells but the one that originates at the marker (C). This decrease is to be expected, since the growth rate is highest near the tip,

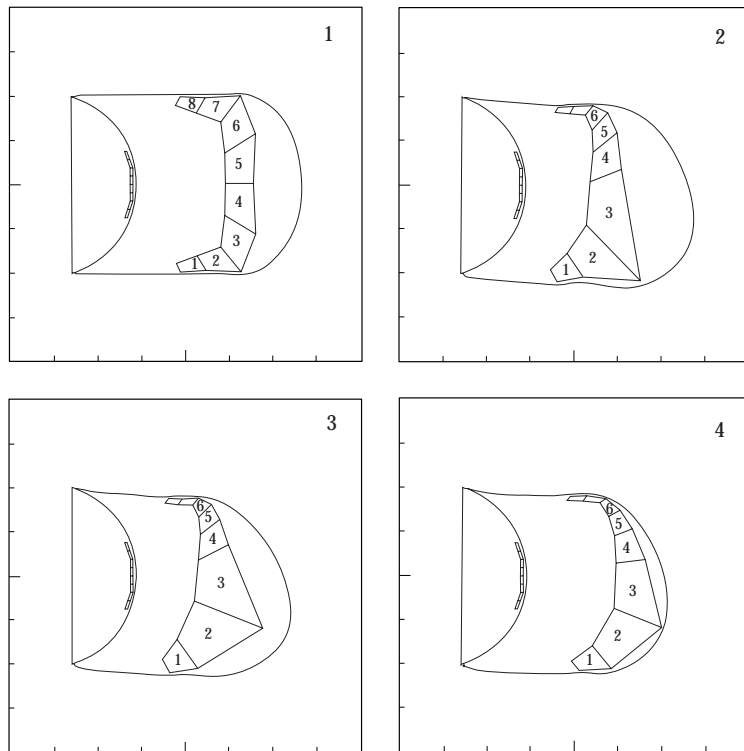


FIG. 10. Blocks 1–8 for simulations 1–4. Each frame shows the initial and final block outlines and limb bud configurations.

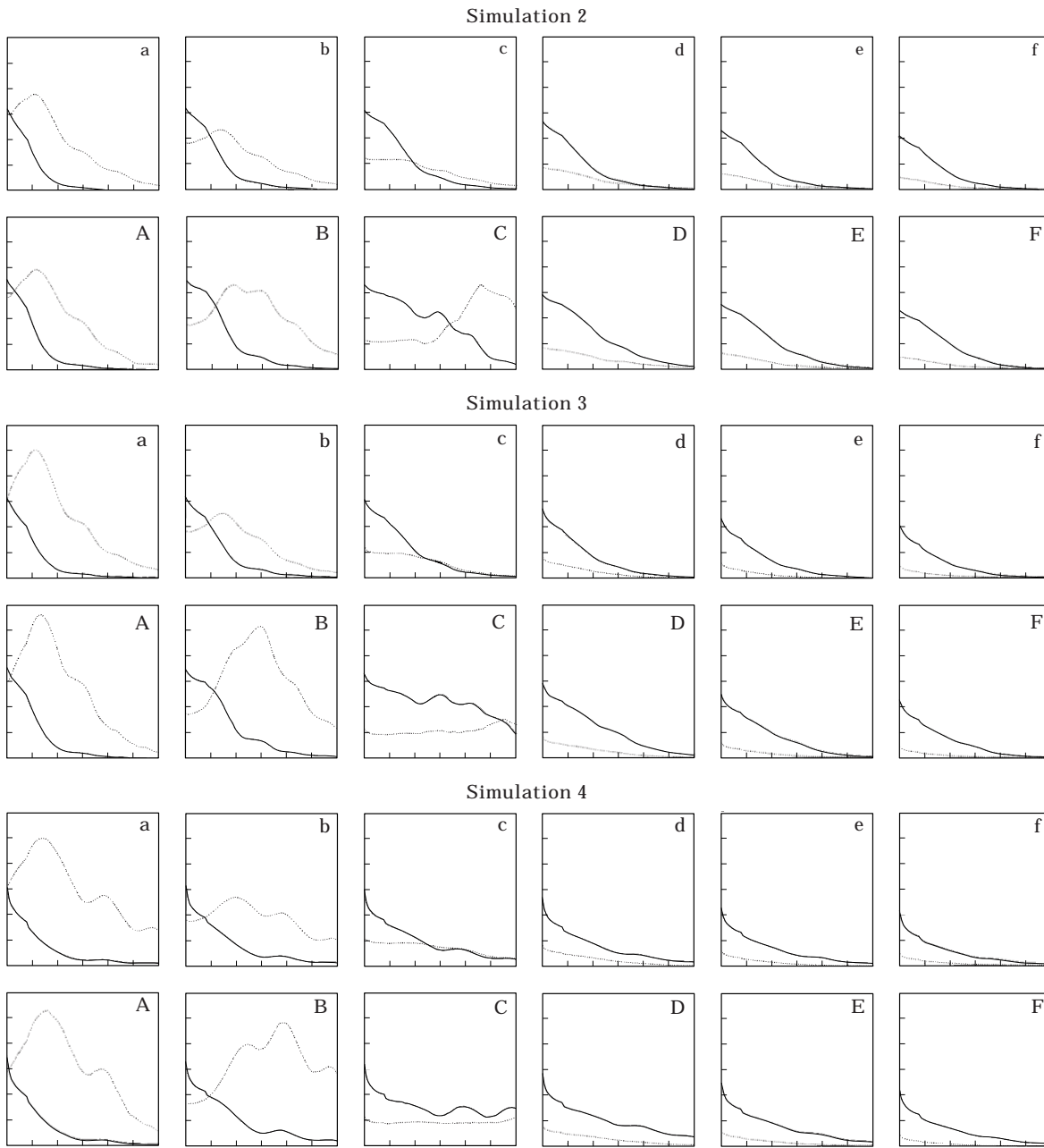


FIG. 11. Concentrations of  $\tilde{z}_1$  (—) and  $\tilde{z}_2$  (···) at the location of the individual fluid markers. The hash marks on the vertical axis of each graph represent equal increments of dimensionless concentration from (0, 6). The hash marks on the horizontal axis represent equal increments in dimensionless time from (0, 1.3125). For each of the simulations shown, the most posterior pair (a, A) is shown at the left of the figure.

and thus the apex grows away from the marked cells. There are small increases at intermediate times for the cell marked C in all simulations because (a) it remains quite close to the tip throughout outgrowth, and (b) its trajectory is displaced posteriorly, and hence toward higher AER factor, especially in Simulation 2.

The temporal profile of the concentration of ZPA factor is quite different for cells that originate in the anterior half as compared with those that originate in the posterior half. In the former the ZPA factor is decreasing in time, as is the AER factor, but cells in the posterior half experience a well-defined temporal maximum of

ZPA factor, and this occurs earliest nearest the ZPA and later toward the midline.

**5. Interpretation Functionals Relating Gene Expression to Morphogen Distributions**

The patterns of gene expression in the growing limb bud, such as those discussed later for *Hox*, may be directly or indirectly related to the spatio-temporal profiles of substances produced in the AER and ZPA. Transduction of an extracellular signal into gene expression usually involves complex signal transduction mechanisms based on intracellular second messengers, and at present the molecular basis of *Hox* gene control has not been elucidated. Thus it is not known if there is a direct connection, but the indirect evidence for a connection is strong enough to justify some theoretical analysis. In this section we suggest several possible interpretation mechanisms by which the morphogen distributions could be translated into patterns of gene expression.

The simplest map between morphogen concentration and gene expression is obtained by making the latter directly dependent on the former. In the previous section we showed that the concentration of the AER factor is a strictly decreasing function of time along most cell trajectories. This fact can be used to define a gene control mechanism as follows. Let us define the progress zone (PZ) as the region in which the concentrations of the AER morphogen and the ZPA factor are above a given threshold, and then cells leave the PZ when either concentration level drops below the respective threshold. Suppose we set the thresholds at  $\tilde{c}_1 = 1$  and  $\tilde{c}_2 = 1$  in Simulation 2 (cf. Fig. 11). Then one sees from that figure that only the cells corresponding to the three posterior-most markers [(a, A)–(c, C)] are ever in the PZ, and these cells leave the PZ in a posterior to anterior sequence in time. This is consistent with the observation that posterior differentiation typically precedes anterior differentiation. Other maps based directly on the morphogen distributions are possible, but we turn next to maps based on a rudimentary form of signal transduction.

In the simplest model we assume that the activation and transcription of the genes in

question depends on the concentration of  $c_1$  and  $c_2$  at the cell site. The gene product  $w_k$ , which is the indicator of gene expression, is produced in each cell according to the differential equation

$$\frac{dw_k}{dt} = f(\tilde{c}_k(t)) - \beta_k w_k \tag{45}$$

where as before,  $\tilde{c}_k(t)$  is the  $k$ -th morphogen concentration in the Lagrangian description, i.e. at the cell site at time  $t$ . We suppose that production of  $w_k$  depends only on the concentration of  $\tilde{c}_k$  and that it is degraded according to first-order kinetics with rate constant  $\beta_k$ . The form of the response function  $f$  is described below. In this model, the production rate of a particular gene product  $w_k$  depends only on the single morphogen  $\tilde{c}_k$ , but a more complex model could be constructed in which the production rates depend on both morphogens.

The solution to (45) is

$$w_k(t) = w_k(0)e^{-\beta_k t} + \int_0^t f(\tilde{c}_k(s))e^{-\beta_k(t-s)} ds. \tag{46}$$

Thus the current concentration of the gene product,  $w_k(t)$ , depends on the entire history of the morphogen concentration  $\tilde{c}_k$  at the cell site. The decay rate of  $w_k$  determines how rapidly the “memory” of past concentrations fades, and the function  $f$  determines how the morphogen concentration is filtered via the signal transduction scheme. The following four characteristic forms for the response function  $f$  will be considered here.

$$f_1 = \frac{\tilde{c}_k}{1 + c_k}$$

$$f_2 = \frac{\tilde{c}_k}{1 + \tilde{c}_k^2}$$

$$f_3 = \frac{\tilde{c}_k^6}{1 + \tilde{c}_k^6}$$

$$f_4 = \frac{\tilde{c}_k^6}{100 + \tilde{c}_k^6}$$

The graphs of these functions are shown in Fig. 12, where one sees that  $f_1$ ,  $f_3$  and  $f_4$  are increasing functions of  $\tilde{c}_k$ ,  $k = 1, 2$ , and each of

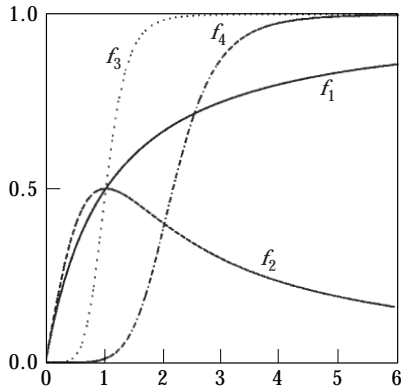


FIG. 12. Graphs of the four functions used in the interpretation schemes.

these saturates at 1. The function  $f_2$  has a single maximum and decays to zero for large  $\tilde{c}_k$ ,  $f_1$  is of Michaelis–Menten form, and  $f_3$  and  $f_4$  are sigmoidal and differ only in the half-maximal concentration. The primary difference between the Michaelis–Menten and sigmoidal functions is in the shape of the function at the toe near  $\tilde{c}_k = 0$ . The sigmoidal functions  $f_3$  and  $f_4$  are intended to approximate “switches” of different sharpness under which the production of  $w_k$  switches rapidly from low to high as  $\tilde{c}_k$  increases. In the following we apply these functionals to the concentration histories in Simulation 2. The conclusions for the other simulations are similar.

We set  $\beta = 10$  and  $w(0) = 0$  and compute the temporal evolution of  $w_k$  for all pairs of fluid markers in the posterior half of the limb. The results for  $f_1$  and  $f_2$  are shown in Fig. 13 and those for  $f_3$  and  $f_4$  are shown in Fig. 14. These figures should be compared with the graphs of  $\tilde{c}_k$  for the same fluid markers shown in Fig. 11. Clearly the graphs of  $w_k$  are much smoother than are those for  $\tilde{c}_k$  because the concentration is smoothed via the integration in eqn (46). Moreover, because the “gene product”  $w_k$  is zero initially, the  $w_k$ s have a pronounced maximum and the time above half-maximal concentration depends strongly on the response function. For example  $f_1$ ,  $f_2$  and  $f_3$  produce relatively broad peaks, and in addition, the location of the peak in time

\* In order to generate these contours, we solve eqn (46) for each of the fluid markers in the limb domain. The concentration data at the irregularly spaced fluid markers is interpolated to the regular grid using the subroutine BIVAR supplied with the NCAR graphics package.

varies significantly with the spatial marker when using  $f_2$  as the filter. It is also evident that, as expected, the switch-like functions  $f_3$  and  $f_4$  enhance the spatial gradients of the gene products along the anterior–posterior axis as compared with those for the morphogen concentrations. In particular, one sees that the anterior–posterior gradient of  $w_2$  is significantly sharper than that of  $c_2$  when using either  $f_3$  or  $f_4$  as the response function.

To better compare our results with experimentally-observed spatial patterns of gene expression, we have also computed the contours of  $w_k$  over the entire limb domain at selected times\*. The contours for  $w_k$  that result from applying the response functions  $f_1$  and  $f_2$  are shown in Figs 15 and 16. The contours in Fig. 15 are suggestive of the *Hoxa* and *Hoxd* expression patterns seen at HH stage 22 (see the Discussion). However, it should be noted that the pattern seen here is qualitatively similar throughout the simulation, whereas the patterns of *Hox* expression in chick limb apparently change significantly during development. Since  $f_1$  is monotone increasing one expects that the concentrations of the  $w_k$ s will be monotone decreasing in the distal to proximal and posterior to anterior directions, and one sees that this is generally the case. In contrast, because  $f_2$  increases rapidly to its maximum at  $w_k = 1$  and falls off gradually at larger concentrations, the region of maximum expression of  $w_k$  does not necessarily coincide with the region of maximum expression of  $c_k$ . In Fig. 16(a), which corresponds to stage 21, the maximum expression of  $w_1$  is found in the subridge proximal to the limb bud apex. In the later stages the high point is found at the apex.

To emphasize the effects of changes in the response functions, we show the  $w_2$  distribution for all four response functions in Fig. 17. To provide a basis for comparison the same concentration levels are shown for all response functions. The functions  $f_1$ ,  $f_3$ , and  $f_4$  are each monotone in  $w_k$  and produce expression patterns with the highest concentrations in  $w_2$  in the ZPA. The concentration levels decrease monotonically in a posterior–distal to anterior–proximal sequence, but this monotonicity is lost in the functional  $f_2$ . Moreover, as can be anticipated from earlier discussion, the expression of  $w_2$  is

much more localized in space for  $f_3$  and  $f_4$ . A comparison of Figs 16 and 17 shows that the qualitative picture of the spatial distribution depends heavily on the decay parameter.

To further emphasize the effect of the decay rate on the spatial distribution of gene product we show the distribution of  $w_2$  for the response function  $f_2$  and a lower decay rate in Fig. 18. One

sees in Fig. 18 that decreasing the decay rate increases the expression domain of  $w_2$ , as expected, but the value of the decay rate can have unexpected effects. One sees that there is a Y-shaped expression domain for  $w_2$ , which is suggestive of what might be used for determining the bifurcation into the radius and ulna, or perhaps later, the digits.

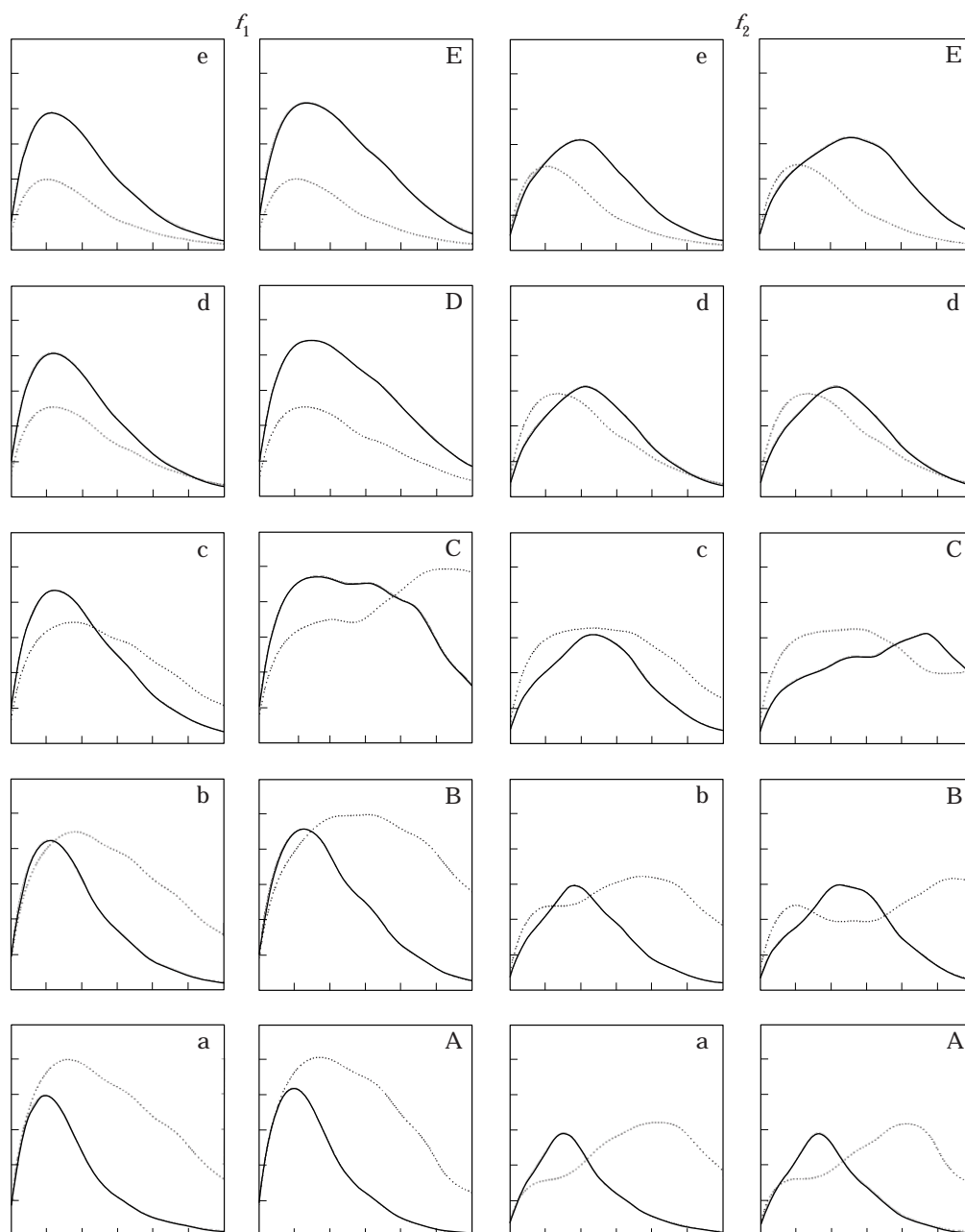


FIG. 13. The temporal profiles of  $w_k$  for simulation 2 at the fluid markers (a, A), (b, B), . . . , (e, E), using the functions  $f_1$  and  $f_2$ . The vertical axis represents the concentration of  $w_k \in [0, 0.1]$ ; the horizontal axis represents dimensionless time for  $t \in [0, 1.3125]$ .

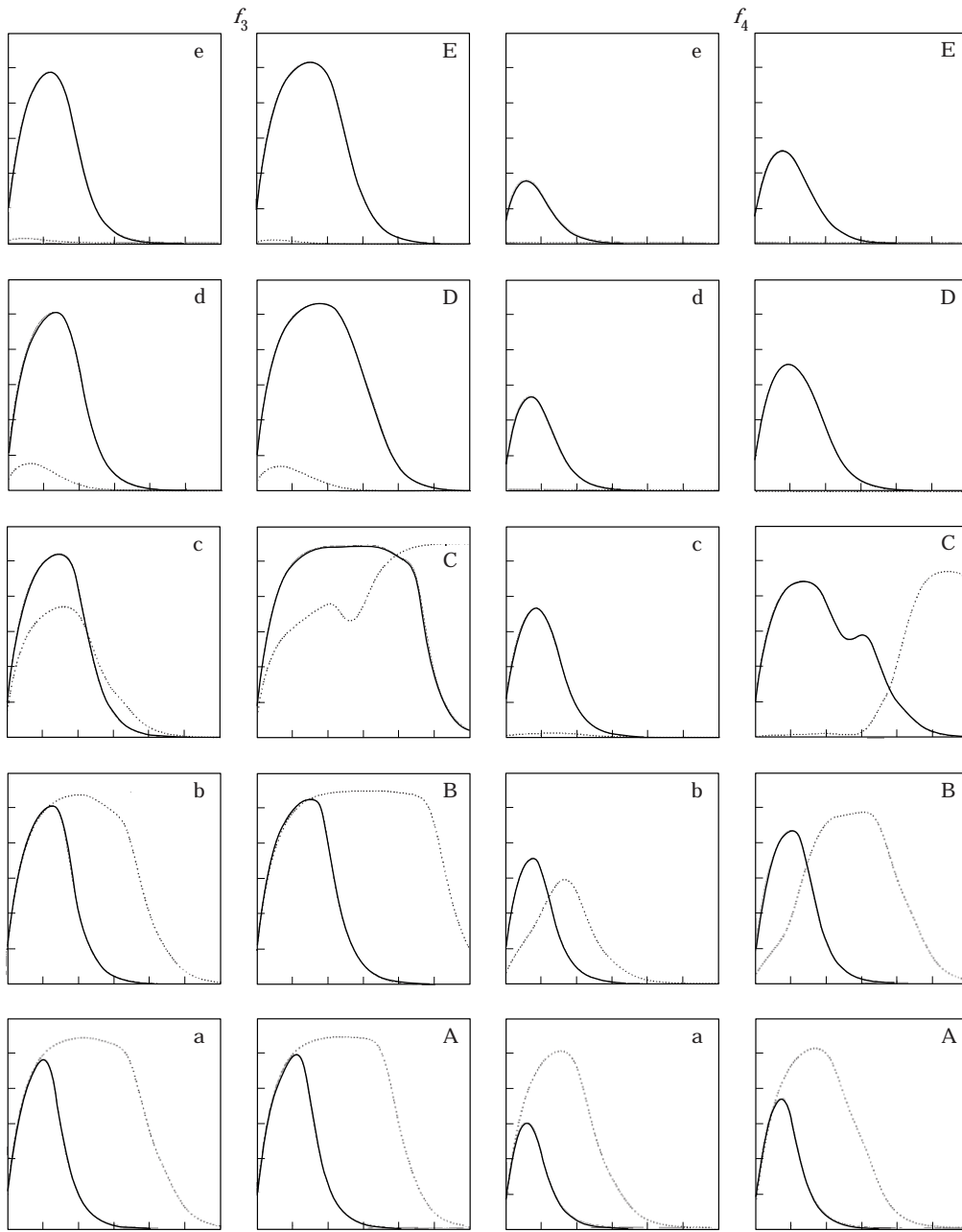


FIG. 14. The temporal profiles of  $w_k$  for simulation 2 at the fluid markers (aA), (bB), . . . , (eE) (ordered top to bottom), using the functions  $f_3$  and  $f_4$ . The vertical axis represents the concentration of  $w_k \in [0, 0.12]$ ; the horizontal axis represents dimensionless time for  $t \in [0, 1.3125]$ .

## 6. Discussion

### 6.1. THE SPATIO-TEMPORAL PATTERN OF GENE EXPRESSION DURING OUTGROWTH

Important features of our model when compared with previous models are the incorporation of outgrowth of the limb bud, the mutual feedback interactions between the AER

and ZPA factors, and the ability to determine the morphogen distributions in two space dimensions as a function of time, both at fixed locations in space, and along cell trajectories in the growing limb. As a result, we can determine the spatial and temporal history of individual cells and cell lines within the changing environment of morphogen concentrations. That the

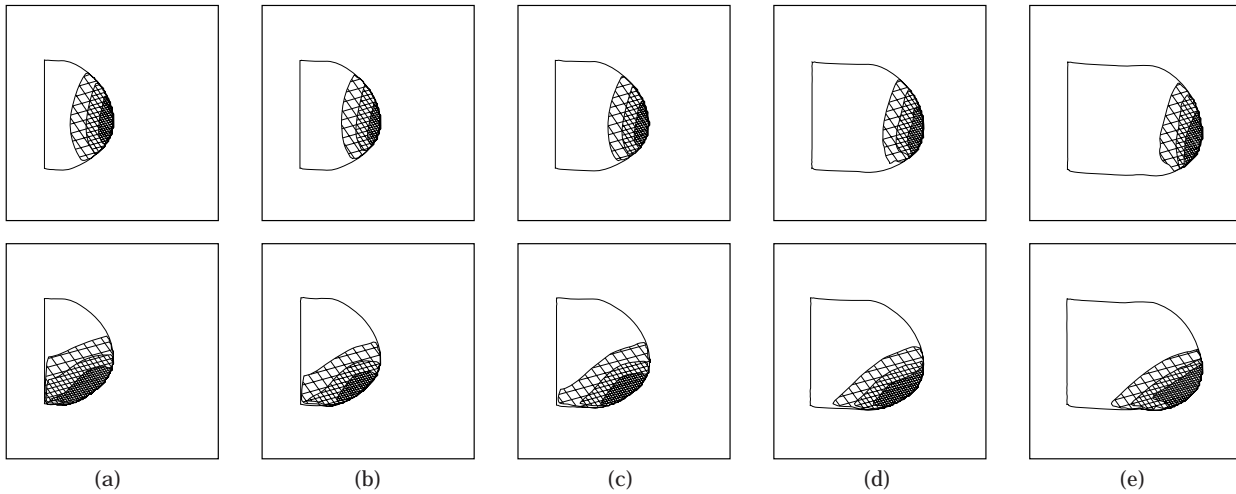


FIG. 15. Concentration contours for  $w_1$  (upper) and  $w_2$  (lower) produced with the functional  $f_1$  at dimensionless times (a) 0.3375; (b) 0.50625; (c) 0.675; (d) 0.9375; (e) 1.2; [real times of (a) 7.8; (b) 11.7; (c) 15.6; (d) 21.7; (e) 27.8 hours and stages (a) 21; (b) 22; (c) 23; (d) 24; (e) 25] in simulation 2. Higher concentration levels are indicated by closer spaced cross hatching. Three dimensionless concentration levels are shown:  $0.02 < w_k < 0.04$ ,  $0.04 < w_k < 0.06$  and  $0.06 < w_k$ .

computational model can give insights into cell and morphogen dynamics *in vivo* is suggested by noting that the fluid marker maps shown in Fig. 8 are qualitatively similar to the fate maps in Bowen *et al.* (1989) in the distal half of the limb bud, and that the block maps shown in Fig. 10 are qualitatively similar to the fate maps shown in Vargesson *et al.* (1997) Fig. 1(B) and 1(G). Because the computations provide information about cell lineage via the fate maps of tissue blocks, as well as the temporal history of morphogen concentration levels within these

tissue blocks (Fig. 11), we can investigate the relationship between cell lineage and gene expression.

In the classical version of the progress zone model discussed in the Introduction, the PZ is regarded as a specialized region within the distal subridge, and the amount of time cells spend in the PZ influences the course of proximal–distal differentiation. In our model we could define the PZ as a region in which the AER growth factor is above a threshold level, and as can be seen in Fig. 7, the contour lines in the AER morphogen

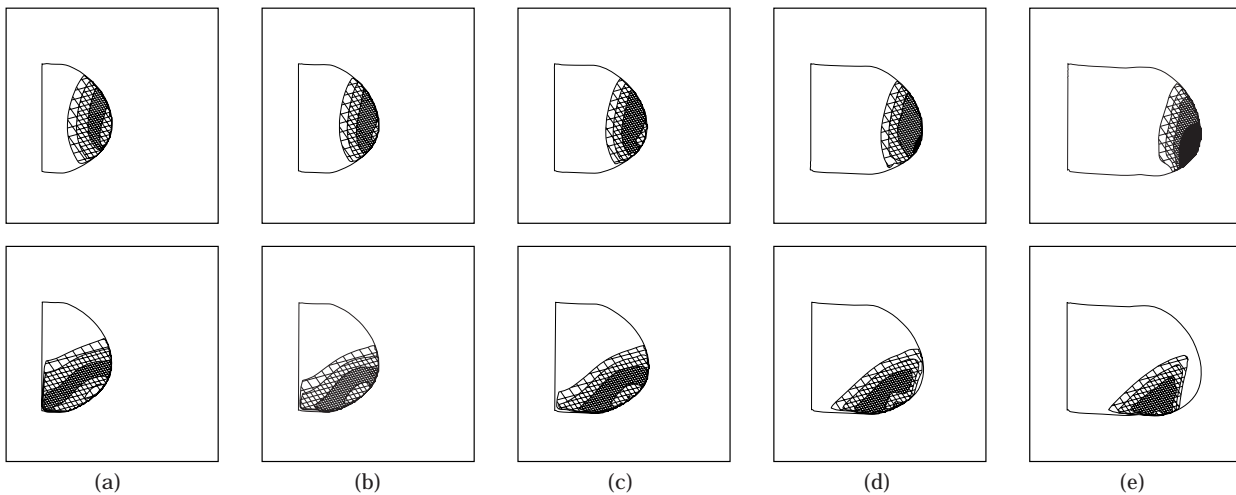


FIG. 16. Concentration levels for  $w_1$  (upper) and  $w_2$  (lower) in simulation 2 produced with the function  $f_2$  at the stages shown in Fig. 15. Four dimensionless concentrations levels are shown:  $0.015 < w_k < 0.020$ ,  $0.020 < w_k < 0.025$ ,  $0.025 < w_k < 0.030$ , and  $0.030 < w_k$ .

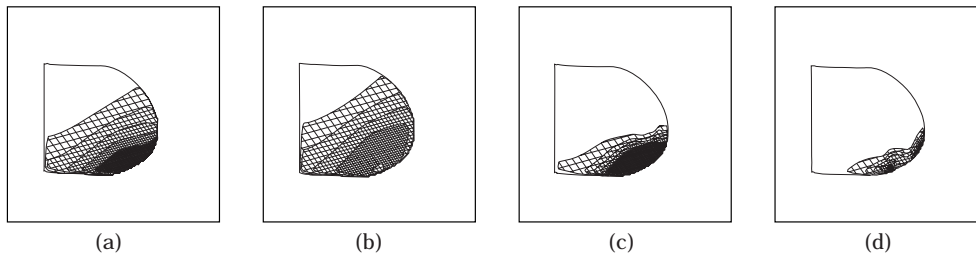


FIG. 17. Concentration levels for  $w_2$  using the four response functions. (a)  $f_1$ ; (b)  $2f_2$ ; (c)  $f_3$ ; (d)  $f_4$ . The contour plots show the solution for simulation 2 at dimensionless time 0.9375 (real time 21.7 hours) corresponding to HH stage 24. Five dimensionless concentrations levels are shown:  $0.04 < w_2 < 0.08$ ,  $0.08 < w_2 < 0.12$ ,  $0.12 < w_2 < 0.16$ ,  $0.16 < w_2 < 0.2$ ,  $0.2 < w_2$ . The parameters for the functions are the same as those used above, except  $\beta = 2.5$ .

$c_1$  define a stable PZ in the distal subridge. Using this definition of the progress zone, one can determine when cells enter and/or leave the progress zone by determining the local concentration of  $c_1$  at the cell site, as shown in Fig. 11. Of course the PZ, and hence the residence time in it, may be determined by a downstream product of the morphogens, and the filtered histories of the morphogen concentrations shown in Figs 13 and 14 illustrate how the time spent in the PZ changes as the definition of the PZ changes.

One of the most important open problems in limb development concerns the relationship between the spatio-temporal pattern of primary signaling molecules such as Sonic and the various growth factors, the patterns of gene expression, and the translation of these patterns into patterns of cell differentiation to cartilage and connective tissue types. Given the complexity of the networks involved in the control of gene expression, the possible redundancy between the effects of homologous genes, and the

paucity of information about the control of cell differentiation, it is not possible to synthesize an integrated scheme at present. However one can address simpler issues, such as the possible relationship between the pattern of signaling molecules and patterns of gene expression. At present most is known about the spatio-temporal pattern of expression of the *Hox* genes, which are thought to be the primary genes involved in the patterning necessary for the proper spatial localization of the cartilage condensations, and therefore we briefly review this information. A listing of many other genes that are known to be expressed in various stages of limb development is given in Tickle & Eichele (1994).

The vertebrate *Hox* genes comprise four complexes of gene clusters, *Hoxa*, *Hoxb*, *Hoxc* and *Hoxd*, and genes in each complex have homologs in each of the other clusters. The patterns of expression of *Hoxa* and *Hoxd* have been most completely mapped, and a summary of the pattern at HH stage 22 is shown in Fig. 19. The five *Hoxd* genes, labeled 9–13 from 3' to 5' on the chromosome, are expressed in a spatially-nested pattern that is centered roughly at the ZPA [cf. Fig. 19(b)] (Izpisua-Belmonte *et al.*, 1991). This spatial pattern of gene expression reflects the temporal order in which genes are read from 3' to 5'. *Hoxd*-9 and *Hoxd*-10 are expressed throughout the prospective limb field at stage 16, *Hoxd*-11 appears at stage 18, and expression of *Hoxd*-12 and *Hoxd*-13 begin thereafter (Nelson *et al.*, 1996).

Our computational results demonstrate that the interaction between two spatially-localized sources of FGF and SHH can produce a stable two-dimensional distribution of each of the morphogens and of secondary gene products as

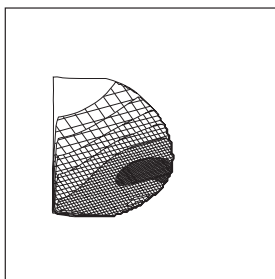


FIG. 18. Concentration levels for  $w_2$  produced with the functional  $2f_2$  at stage 23, but with a decay rate of  $\beta = 1$ . Seven contours levels are shown: (0.04, 0.08), (0.08, 0.12), (0.12, 0.16), (0.16, 0.20), (0.20, 0.24), (0.24, 0.28), (0.28, 0.32).

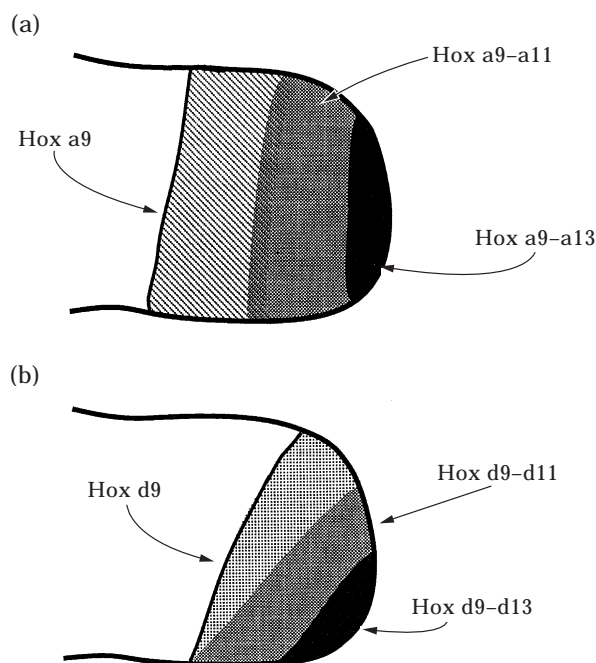


FIG. 19. A schematic of the spatial pattern of *Hoxa* (a) and *Hoxd* (b). After Robertson & Tickle (1997).

well. This morphogenetic landscape could be the basis of a stable positional information system available to the cells over stages 19–25. Although the level sets of the morphogen distributions may not be identified directly with *Hoxa* or *Hoxd* expression, their existence does allow the possibility of a stable positional information system based on interdependent morphogen gradients in two spatial directions. The level sets of the morphogen distributions are also qualitatively similar to the distribution of *Hoxa* and *Hoxd* expression, at least at some stages.

Vargesson *et al.* (1997) have demonstrated that gene expression may depend on both cell lineage and morphogen concentration levels. In that study a lipophilic dye was injected into stage 20 wing buds under the AER and examined later at stage 28. At stage 20 the expression of *Hoxd*-13 is localized in the posterior–distal mesenchyme of the limb bud, but by stage 28 the expression domain has expanded considerably in the anterior direction. Conceivably the expansion of this expression domain could be due entirely to cell growth, as would be predicted by the fate maps of tissue blocks. However, it was found that labeled cells on the proximal periphery at stage 20 do not express the gene at

stage 28, and high concentration levels of FGF may be required for the continued expression of this gene. The results of our computational model are in qualitative agreement with this conclusion, in the sense that cells of the same lineage will nonetheless experience different temporal histories of morphogen exposure.

## 6.2. FUTURE WORK

As we stated earlier, our objective here is not only to study the effects of spatial localization of the ZPA and the AER, and of the coupling between them, but also to develop a computational tool that can be used to investigate the effects of experimental interventions during limb development, and to explore various hypothetical maps between morphogen distributions and gene expression. In future work we plan to extend the model to three space dimensions and to explore some of the grafting and blocking experiments that have been done. We also plan to investigate the interactions between the major known signaling pathways, to develop a better model for the viscoelastic properties of cells, and to include chemotactic motion of cells.

Supported in part by an NSF Postdoctoral Research Fellowship and NSF grant DMS 9805501 to R. Dillon and by NIH Grant #GM21923 to H. Othmer.

## REFERENCES

- ALLEN, F., TICKLE, C. & WARNER, A. (1990). The role of gap junctions in patterning of the chick limb bud. *Development* **108**, 623–634.
- BACHELOR, G. K. (1973). *An Introduction to Fluid Mechanics*. Cambridge: Cambridge University Press.
- BELLAÏCHE, Y., THE, I. & PERRIMON, N. (1998). *Tout-velu* is a *Drosophila* homologue of the putative tumour suppressor *EXT-1* and is needed for Hh diffusion. *Nature* **394**, 85–88.
- BOWEN, J., HINCHLIFFE, J. R., HORDER, T. J. & REEVE, A. M. F. (1989). The fate map of the chick forelimb-bud and its bearing on hypothesized developmental control mechanisms. *Anat. Embryol.* **179**, 269–283.
- COHN, M. J., IZPISÚA-BELMONTE, J. C., ABUD, H. & HEATH, J. K. (1995). Fibroblast growth factors induce additional limb development from the flank of chick embryos. *Cell* **80**(5), 739–746.
- CROSSLEY, P. H. & MARTIN, G. R. (1995). The mouse gene *Fgf-8* encodes a family of polypeptides and is expressed in regions that direct outgrowth and patterning in the developing embryo. *Development* **121**, 439–451.

- CROSSLEY, P. H., MINOWADA, G., MACARTHUR, C. A. & MARTIN, G. R. (1996). Roles for FGF8 in the induction, initiation, and maintenance of chick limb development. *Cell* **84**(1), 127–136.
- DUPREZ, D. M., KOSTAKOPOULOS, K., FRANCIS-WEST, P. H., TICKLE, C. & BRICKELL, P. M. (1996). Activation of Fgf-4 and HoxD gene expression by BMP-2 expressing cells in the developing chick limb. *Development* **122**, 1821–1828.
- FUNG, Y. C. (1993). *Biomechanics: Mechanical Properties of Living Tissues*. Berlin: Springer-Verlag.
- GRIESHAMMER, U., MINOWADA, G., PISENTI, J. M., ABBOTT, U. K. & MARTIN, G. R. (1996). The chick *limbless* mutation causes abnormalities in limb bud dorsal–ventral patterning: implications for the mechanism of apical ridge formation. *Development* **122**, 3851–3861.
- HARAMIS, A. G., BROWN, J. M. & ZELLER, R. (1995). The *limb deformity* mutation disrupts the SHH/FGF-4 feedback loop and regulation of 5' *HoxD* genes during limb pattern formation. *Development* **121**, 4237–4245.
- HELMS, J., THALLER, C. & EICHELE, G. (1994). Relationship between retinoic acid and *sonic hedgehog*, two polarizing signals in the chick wing bud. *Development* **120**, 3267–3274.
- HINCHLIFFE, J. R. & GRIFFITHS, P. J. (1984). Experimental analysis of the control of cell death in chick limb bud development. In: *Society for Experimental Biology Seminar Series, Vol. 25. Cell Ageing and Cell Death; Meeting* (Davies I. & Sigee, D. C., eds) pp. 223–242. Cambridge, England, New York: Cambridge University Press.
- HONIG, L. S. & SUMMERBELL, D. (1985). Maps of strength of positional signaling activity in the developing chick wing bud. *J. Embryol. Exp. Morphol.* **87**, 163–174.
- HORNBRUCH, A. & WOLPERT, L. (1991). The spatial and temporal distribution of polarizing activity in the flank of the pre-limb-bud stages in the chick embryo. *Development* **111**, 725–731.
- IZPISÚA-BELMONTE, J. C., TICKLE, C., DOLLÉ, P., WOLPERT, L. & DUBOULE, D. (1991). Expression of the homeobox Hox-4 genes and specification of position in chick wing development. *Nature* **350**, 585–589.
- JAVOIS, L. C. & ITEN, L. E. (1981). Position of origin of donor posterior chick wing bud tissue transplanted to an anterior host site determines the extra structures formed. *Dev. Biol.* **82**(2), 329–342.
- JAVOIS, L. C. & ITEN, L. E. (1986). The handedness and origin of supernumerary limb structures following 180 degree rotation of the chick wing bud on its stump. *J. Embryol. Exp. Morphol.* **91**, 135–152.
- JOHNSON, R. L. & TABIN, C. J. (1997). Molecular models for vertebrate limb development. *Cell* **90**, 979–990.
- KUHLMAN, J. & NISWANDER, L. (1997). Limb deformity proteins: role in mesodermal induction of the apical ectodermal ridge. *Development* **124**(1), 133–139.
- LAUFER, E., NELSON, C. E., JOHNSON, R. L., MORGAN, B. A. & TABIN, C. (1994). *Sonic hedgehog* and *Fgf-4* act through a signaling cascade and feedback loop to integrate growth and patterning in the developing limb bud. *Cell* **79**, 993–1003.
- LEVEQUE, R. J. & LI, Z. (1994). The immersed interface method for elliptic equations with discontinuous coefficients and singular sources. *SIAM J. Numer. Anal.* **31**, 1019–1044.
- LU, H.-C., REVELLI, J.-P., GOERING, L., THALLER, C. & EICHELE, G. (1997). Retinoid signaling is required for the establishment of a ZPA and for the expression of Hoxb-8, a mediator of ZPA formation. *Development* **124**(9), 1643–1651.
- MACCABE, J. A., MACCABE, A. B., ABBOTT, U. K. & MCCARREY, J. R. (1975). Limb development in *Diplopodia*: a polydactylous mutation in the chicken. *J. Exp. Zool.* **191**, 383–392.
- MADEN, M., ONG, D. E., SUMMERBELL, D. & CHYTL, F. (1988). Spatial distribution of cellular protein binding to retinoic acid in the chick limb bud. *Nature* **335**, 733–735.
- MAINI, P. K. & SOLURSH, M. (1991). Cellular mechanisms of pattern formation in the developing limb. *Int. Rev. Cytol.* **129**, 91–133.
- MARIGO, V., JOHNSON, R. L., VORTKAMP, A. & TABIN, C. J. (1996). Sonic hedgehog differentially regulates expression of GL1 and GL13 during limb development. *Dev. Biol.* **180**(1), 273–283.
- MEHTA, P., BERTRAM, J. S. & LOEWENSTEIN, W. R. (1989). The actions of retinoids on cellular growth correlate with their actions on gap junctional communication. *J. Cell Biol.* **108**, 1053–1065.
- MEINHARDT, H. (1982). *Models of Biological Pattern Formation*. London: Academic Press.
- MEINHARDT, H. (1983). A boundary model for pattern formation in vertebrate limbs. *J. Embryol. Exp. Morphol.* **76**, 115–137.
- MICHAUD, J. L., LAPOINTE, F. & LE DOUARIN, N. M. (1997). The dorsoventral polarity of the presumptive limb is determined by signals produced by the somites and by the lateral somatopleure. *Development* **124**(8), 1453–1463.
- MORTON, K. W. & MAYERS, D. F. (1994). *Numerical Solution of Partial Differential Equations*. Cambridge: Cambridge University Press.
- NELSON, C. E., MORGAN, B. A., BURKE, A. C., LAUFER, E., DIMAMBRO, E., MURTAUGH, L. C., GONZALES, E., TESSAROLLO, L., PARADA, L. F. & TABIN, C. (1996). Analysis of *Hox* gene expression in the chick limb bud. *Development* **122**, 1449–1466.
- NISWANDER, L. (1997). Limb mutants: what can they tell us about normal limb development? *Curr. Opin. Gen. Dev.* **7**, 530–536.
- NISWANDER, L. & MARTIN, G. R. (1993). Mixed signals from the AER: FGF-4 and BMP-2 have opposite effects on limb outgrowth. In: *Limb Development and Regeneration* pp. 625–633. New York: Wiley-Liss.
- OGURA, T., ALVAREZ, I. S., VOGEL, A., RODRIGUEZ, C., EVANS, R. M. & BELMONTE, J. C. I. (1996). Evidence that Shh cooperates with a retinoic acid inducible co-factor to establish ZPA-like activity. *Development* **122**, 537–542.
- OHUCHI, H., NAKAGAWA, T., YAMAMOTO, A., ARAGA, A., OHATA, T., ISHIMARU, Y., YOSHIOKA, H., KUWANA, T., NOHNO, T., YAMASAKI, M., ITOH, N. & NOJI, S. (1997). The mesenchymal factor, FGF10, initiates and maintains the outgrowth of the chick limb bud through interaction with FGF8, an apical ectodermal factor. *Development* **124**(11), 2235–2244.
- OSTER, G. F., MURRAY, J. D. & HARRIS, A. K. (1983). Mechanical aspects of mesenchymal morphogenesis. *J. Embryol. Exp. Morph.* **78**, 83–125.
- PAUTOU, M. P. (1973). Analyse de la morphogenese du pied des Oiseaux a l'aide de melange cellulaires interspecificques. I. Etude morphologique. *J. Embryol. Exp. Morphol.* **29**, 175–196.
- PESKIN, C. S. (1977). Numerical analysis of blood flow in the heart. *J. Comp. Phys.*, **25**, 220–252.

- PESKIN, C. S. & McQUEEN, D. M. (1995). A general method for the computer simulation of biological systems interacting with fluids. In: *Biological Fluid Dynamics* (Ellington, C. P. & Pedley, T. J., eds). Company of Biologists, Ltd.
- PHILIPS, H. M. & STEINBERG, M. S. (1969). Equilibrium measurements of embryonic chick cell adhesiveness. I. Shape equilibrium in centrifugal fields. *Proc. Nat. Acad. Sci. U.S.A.*, **64**, 121–127.
- PHILIPS, H. M. & STEINBERG, M. S. (1978). Embryonic tissues as elasticoviscous liquids. I. Rapid and slow shape changes in centrifuged cell aggregates. *J. Cell Sci.* **30**, 1–20.
- PHILIPS, H. M., STEINBERG, M. S. & LIPTON, B. H. (1977). Embryonic tissues as elasticoviscous liquids. II. Direct evidence for cell slippage in centrifuged aggregates. *Dev. Biol.* **59**, 124–134.
- RIDDLE, R. D., JOHNSON, R. L., LAUFER, E. & TABIN, C. (1993). *Sonic hedgehog* mediates polarizing activity of the ZPA. *Cell* **75**, 1401–1416.
- ROBERTSON, K. E. & TICKLE, C. (1997). Recent molecular advances in understanding vertebrate limb development. *Br. J. Plastic Surgery* **50**(2), 109–115.
- RUIZ I ALTABA, A. (1994). Later. *Trends Neurosci.* **17**, 233–243.
- SEARLS, R. L. & JANNERS, M. Y. (1971). The initiation of limb bud outgrowth in the embryonic chick. *Dev. Biol.* **24**, 198–213.
- SMITH, S. M., PANG, K., SUNDIN, O., WEDDEN, S. E., THALLER, C. & EICHELE, G. (1989). Molecular approaches to vertebrate limb morphogenesis. *Development (Suppl)*, 121–131.
- SOLURSH, M. & JENSEN, K. L. (1988). The accumulation of basement membrane components during the onset of chondrogenesis and myogenesis in the chick wing bud. *Development* **104**(1), 41–50.
- STARK, R. J. & SEARLS, R. L. (1973). A description of chick wing bud development and a model of limb morphogenesis. *Dev. Biol.* **33**, 138–153.
- SUMMERBELL, D. (1974a). Interaction between the proximo-distal and antero-posterior coordinates of positional value during the specification of positional information in the early development of the chick limb-bud. *J. Embryol. Exp. Morphol.* **32**, 227–237.
- SUMMERBELL, D. (1974b). A quantitative analysis of the effect of excision of the AER from the chick limb-bud. *J. Embryol. Exp. Morphol.* **32**, 651–660.
- SUMMERBELL, D. (1977). Regulation of deficiencies along the proximal distal axis of the chick wing-bud: a quantitative analysis. *J. Embryol. Exp. Morphol.* **41**, 137–159.
- SUMMERBELL, D. (1979). The zone of polarizing activity: evidence for a role in normal chick morphogenesis. *J. Embryol. Exp. Morphol.* **50**, 217–233.
- SUMMERBELL, D. (1981). Control of growth and the development of pattern across the anteroposterior axis of the chick limb bud. *J. Embryol. Exp. Morphol.* **63**, 161–180.
- SUMMERBELL, D. & LEWIS, J. H. (1975). Time, place and positional value in the chick limb-bud. *J. Embryol. Exp. Morphol.* **33**, 621–643.
- SUMMERBELL, D., LEWIS, J. H. & WOLPERT, L. (1973). Positional information in chick limb morphogenesis. *Nature* **244**, 492–496.
- THALLER, C. & EICHELE, G. (1987). Identification and spatial distribution of retinoids in the developing chick limb bud. *Nature* **327**, 625–628.
- TICKLE, C. (1980). The polarizing region and limb development. In: *Development in Mammals* (Johnson, M. H., ed.), vol. 4, pp. 101–136. Amsterdam: Elsevier/North-Holland Biomedical Press.
- TICKLE, C. & EICHELE, G. (1994). Vertebrate limb development. In: *Annual Review of Cell Biology* pp. 121–152. Annual Reviews, Inc.
- TICKLE, C., LEE, J. & EICHELE, G. (1985). A quantitative analysis of the effect of all-trans-retinoic acid on the pattern of chick wing development. *Dev. Biol.* **109**, 82–95.
- TICKLE, C., SUMMERBELL, D. & WOLPERT, L. (1975). Positional signalling and specification of digits in chick limb morphogenesis. *Nature* **254**, 199–202.
- VARGESSON, N., CLARKE, J. D., VINCENT, K., COLES, C., WOLPERT, L. & TICKLE, C. (1997). Cell fate in the chick limb bud and relationship to gene expression. *Development* **124**(10), 1909–1918.
- VOGEL, A. & TICKLE, C. (1993). FGF-4 maintains polarizing activity of posterior limb bud cells *in vivo* and *in vitro*. *Development* **119**, 199–206.
- VOGEL, A., RODRIGUEZ, C. & IZPISÚA-BELMONTE, J.-C. (1996). Involvement of FGF-8 in initiation, outgrowth and patterning of the vertebrate limb. *Development* **122**, 1737–1750.
- WILBY, O. K. & EDE, D. A. (1975). A model for generating the pattern of cartilage skeletal elements in the embryonic chick limb. *J. theor. Biol.* **52**, 199–217.
- WOLPERT, L. (1969). Positional information and the spatial pattern of cellular differentiation. *J. theor. Biol.* **25**, 1–47.
- WOLPERT, L. (1976). Mechanisms of limb development and malformation. *Br. Med. J.* **32**, 65–70.
- WOLPERT, L. (1987). An introduction to cells. *Br. Med. J.* **295**(6604), 987–988.
- WOLPERT, L. & HORNBRUCH, A. (1990). Double anterior chick limb buds and models for cartilage rudiment specification. *Development* **109**, 961–966.
- WOLPERT, L., LEWIS, J. & SUMMERBELL, D. (1975). Morphogenesis of the vertebrate limb. *Ciba Symp.* **29**, 95–130.
- ZWILLING, E. (1961). Limb morphogenesis. *Adv. Morphogen.* **1**, 301–330.

## APPENDIX

The rectangular fluid domain is discretized using a uniform rectangular grid. The fluid variables ( $\mathbf{u}$ ,  $p$ ,  $\mathbf{F}$ ,  $S$ ) are discretized and defined at the grid points. The limb bud boundary is also discretized and represented by a finite number of points  $\mathbf{X}_p$ ,  $p = 1, \dots, N$ , but in general the immersed boundary points  $\mathbf{X}_p$  do not coincide with points of the fluid grid. The boundary forces  $\mathbf{f}_p$  are defined at the points  $\mathbf{X}_p$ , and interpolation between the immersed boundary points and the fluid grid is effected by means of a discrete  $\delta$ -function given below. The concentration of chemical species  $c$  is defined on the same grid as the fluid variables. Since the computational fluid domain is rectangular we are able to use Fast

Fourier Transform methods for time-stepping the fluid equations.

The algorithm for numerical solution of the coupled fluid-chemical system can be summarized as follows. At the beginning of each time step  $n$  we have the fluid velocity field  $\mathbf{u}^n$ , the locations  $\mathbf{X}_p^n$  of the immersed boundary points, and the chemical concentration field  $\mathbf{c}^n$ . In order to update these values during this time step we do the following.

1. Calculate the force density  $\mathbf{f}_p^n$  at each immersed boundary point.
2. Interpolate the forces to the grid to determine the force density  $\mathbf{F}$  [eqn (4)].
3. Calculate the local growth rate  $S^n = S(\mathbf{c}^n)$ .
4. Solve the Navier–Stokes eqns (1–2) for  $\mathbf{u}^{n+1}$ .
5. Interpolate the fluid velocity field to each immersed boundary point and move that point at its local fluid velocity to obtain  $\mathbf{X}_p^{n+1}$  [eqn (3)].
6. Solve the advection–diffusion–reaction eqn (5) for  $\mathbf{c}^{n+1}$ .

### A.1. Elastic Boundary Forces

The ectodermal boundary of the two-dimensional limb bud is modeled by a discrete set of immersed boundary points  $\mathbf{X}_p$  for  $p = 1, \dots, N(t)$ . The location of each point is time dependent. Each immersed boundary point  $\mathbf{X}_p$  is connected to its neighbors  $\mathbf{X}_{p-1}$  and  $\mathbf{X}_{p+1}$  by elastic forces of the form

$$\mathbf{f}_k = \sum_{\substack{p=k-1 \\ p \neq k}}^{k+1} \frac{S_1(\|\mathbf{X}_k - \mathbf{X}_p\| - L_0)(\mathbf{X}_k - \mathbf{X}_p)}{\|\mathbf{X}_k - \mathbf{X}_p\|}. \quad (\text{A.1})$$

where  $S_1$  is a spring stiffness constant and  $L_0$  is the resting length. The initial spacing between adjacent pairs of immersed boundary points is also given by the resting length  $L_0$  and is one-half the mesh width of the two-dimensional fluid domain. The immersed boundary points along the proximal boundary are also tethered to fixed points in space via elastic spring, and thus these

points are subject to an additional force of the form

$$\mathbf{f}_k^2 = S_2(\mathbf{X}_k - \mathbf{X}_k^0), \quad (\text{A.2})$$

where  $S_2$  is a spring stiffness constant and  $\mathbf{X}_k^0$  is the initial location of a proximal boundary point  $\mathbf{X}_k$ . The tethering force  $\mathbf{f}_k^2 = 0$  at all immersed boundary points away from the proximal boundary.

Each immersed boundary point along the posterior boundary is also connected via an elastic spring force to an immersed boundary point on the anterior boundary. If we label the set of non-proximal boundary points  $(\mathbf{X}_1, \dots, \mathbf{X}_M)$ , from the lower left corner of the limb bud counterclockwise around the limb to the upper left corner, we form an elastic link between pairs  $(\mathbf{X}_1, \mathbf{X}_M)$ ,  $(\mathbf{X}_2, \mathbf{X}_{M-1})$ ,  $\dots$ ,  $(\mathbf{X}_{M/2-1}, \mathbf{X}_{M/2+1})$ . The transverse force at a posterior immersed boundary point  $\mathbf{X}_k$  is derived from an equation of the form

$$\mathbf{f}_k^3 = S_3(\|\mathbf{X}_k - \mathbf{X}_p\| - D_w)(\mathbf{X}_k - \mathbf{X}_p)/\|\mathbf{X}_k - \mathbf{X}_p\|. \quad (\text{A.3})$$

where  $p = M - k + 1$ . The spring constants  $S_3$  are taken to be zero unless the distance between the pair of points is greater than  $D_w$ , the nominal limb bud width. These transverse forces constrain the limb so that it elongates along the proximal distal axis rather than ballooning as the limb bud grows.

The total elastic force at each immersed boundary point is the sum  $\mathbf{f}_k = \sum_{j=1}^3 \mathbf{f}_k^j$ . These forces  $\mathbf{f}$  are interpolated to the two-dimensional numerical fluid grid points by a discrete version of eqn (4). The interpolation is based on an approximate delta function of the form  $\delta_h(\mathbf{x}) = d(x) d(y)$  where  $h$  is the mesh width and

$$d(r) = \begin{cases} \frac{1}{4h} \left( 1 + \cos \frac{\pi r}{2h} \right) & |r| < 2h \\ 0 & |r| \geq 2h. \end{cases} \quad (\text{A.4})$$

We refer the reader to Peskin (1977) for further details.

As the limb bud expands, the immersed boundary points become more widely spaced. During the simulation, we introduce a new

boundary point between an adjacent pair if the elastic link exceeds a prescribed length.

## A.2. Numerical Solution of the Navier–Stokes Equations

The numerical method for solving the Navier–Stokes eqns (1)–(2) is similar to the method described in Peskin & McQueen (1995). Our model includes an additional term in eqn (1) due to the distributed source  $S$  in the continuity eqn (2). Equations (1)–(2) are discretized on a regular rectangular grid of with mesh width  $h$

$$\begin{aligned} \rho \left( \frac{\mathbf{u}^{n+1} - \mathbf{u}^n}{\Delta t} + \sum_{s=1}^2 u_s^n D_s^\pm \mathbf{u}^n \right) &= -\mathbf{D}^0 p^{n+1} \\ &+ \mu \left( \sum_{s=1}^2 D_s^+ D_s^- \mathbf{u}^{n+1} + 1/3 \mathbf{D}^0 S^n \right) + \rho F^n \\ \mathbf{D}^0 \cdot \mathbf{u}^{n+1} &= S^n \end{aligned} \quad (\text{A.5})$$

where  $S^n = S(\mathbf{c}^n)$ ,  $D_s^+$ ,  $D_s^-$  are the forward and backward divided difference operators for  $s = x, y$ ,  $\mathbf{D}^0$  is the centered divided difference,  $\mathbf{D}^0 \cdot$  is the center divided difference divergence operator and  $D_s^\pm$  is the upwind divided difference (Peskin & McQueen, 1995). Equation (A.5) can be rewritten as:

$$\begin{aligned} \left( I - \frac{\mu \Delta t}{\rho} \sum_{s=1}^2 D_s^+ D_s^- \right) \mathbf{u}^{n+1} + \frac{\Delta t}{\rho} \mathbf{D}^0 p^{n+1} &= v^n \\ \mathbf{D}^0 \cdot \mathbf{u}^{n+1} &= S^n \end{aligned} \quad (\text{A.6})$$

with

$$\begin{aligned} v^n &= \left( I - \Delta t \sum_{s=1}^2 u_s^n D_s^\pm \right) \mathbf{u}^n + \frac{\mu \Delta t}{3\rho} \mathbf{D}^0 S^n \\ &+ \Delta t F^n. \end{aligned} \quad (\text{A.7})$$

Equation (A.6) is a constant-coefficient system of difference equations in the unknowns  $(\mathbf{u}^{n+1}, p^{n+1})$ . We can define the discrete Fourier

transformation of the grid function  $\phi$  on the spatial domain  $(0, L)^2$  by

$$\hat{\phi}_{k_1, k_2} = \sum_{j_1, j_2=0}^{N-1} \exp(-i(2\pi/N)(j_1 k_1 + j_2 k_2)) \phi_{j_1 j_2} \quad (\text{A.8})$$

for  $0 \leq k_1, k_2 \leq N-1$  and  $L = Nh$ . With this definition, the discrete Fourier transform of eqn (A.6) is given by:

$$\begin{aligned} \left( 1 + \frac{4\mu \Delta t}{\rho h^2} \sum_{s=1}^2 \sin^2(\pi k_s/N) \right) (u_s)_{k_1 k_2}^{n+1} \\ + \frac{i \Delta t}{\rho h} \sin(2\pi k_s/N) p_{k_1 k_2}^{n+1} &= (v_s)_{k_1 k_2}^n \\ \frac{i}{h} \sum_{s=1}^2 \sin\left(\frac{2\pi k_s}{N}\right) (u_s)_{k_1 k_2} &= \hat{S}_{k_1 k_2}^n. \end{aligned} \quad (\text{A.9})$$

We can now multiply eqn (A.9) by

$$\frac{i}{h} \sin\left(\frac{2\pi k_s}{N}\right) \quad (\text{A.10})$$

and sum over  $s = 1, 2$ , to obtain

$$\begin{aligned} p_{k_1 k_2}^{n+1} &= \left[ \left( 1 + \frac{4\mu \Delta t}{\rho h^2} \sum_{s=1}^2 \sin^2(\pi k_s/N) \right) \hat{S}_{k_1 k_2}^n - \frac{i}{h} \sum_{s=1}^2 \right. \\ &\times \left. \sin(2\pi k_s/N) (v_s)_{k_1 k_2} \right] / \left[ \frac{\Delta t}{\rho h^2} \sum_{s=1}^2 \sin^2(2\pi k_s/N) \right]. \end{aligned} \quad (\text{A.11})$$

With  $p$  known, we can solve eqn (A.9) for  $u$  to obtain:

$$(u_s)_{k_1 k_2}^{n+1} = \frac{(v_s)_{k_1 k_2}^n - \frac{i \Delta t}{\rho h} \sin(2\pi k_s/N) p_{k_1 k_2}^{n+1}}{1 + \frac{4\mu \Delta t}{\rho h^2} \sum_{s=1}^2 \sin^2(\pi k_s/N)}. \quad (\text{A.12})$$

Note that the denominator in eqn (A.11) is zero for  $(k_1, k_2) = (0, 0)$ ,  $(0, N/2)$ ,  $(N/2, 0)$ , or  $(N/2, N/2)$ . For these values of  $(k_1, k_2)$  we can solve eqn (A.9) directly for  $(u_s)_{k_1 k_2}$  since the term involving  $p_{k_1 k_2}$  is zero. This is equivalent to setting  $p_{k_1 k_2} = 0$  in eqn (A.12). Once  $\mathbf{u}^{n+1}$  is

computed, we make no further use of the  $p^{n+1}$  and obtain the fluid velocity field  $\mathbf{u}^{n+1}$  using the inverse discrete Fourier transform.

This model might be formulated for the Stokes equations [obtained from eqns (1)–(2) by setting the left-hand side of eqn (2) to zero]. However, for a solution to exist on a periodic domain, the integral of  $F$  over the domain must be zero. This condition will not necessarily hold if a portion of the limb bud immersed boundary is tethered as it is in our model. Thus a time dependent equation must be employed. In the method used here, the computational cost of including the advective term  $(\mathbf{u} \cdot \nabla)\mathbf{u}$  is minimal since this term is evaluated at the previous time step.

### A.3. Solution of the Advection–Reaction–Diffusion Equations

The irregularly shaped-moving boundary of the growing limb bud creates special difficulties for the numerical solution of the advection–reaction–diffusion eqns (5). The model requires Neumann (zero-flux) boundary conditions for the chemical species at this interface. We solve these equations on the same grid as the fluid equations. At regular grid points within the limb bud domain, we use a standard five-point stencil for the Laplacian  $\nabla^2 c$ . At irregular grid points at least one of the grid points in the standard five-point stencil lies outside of the limb bud domain. As a result, the irregular grid points require special treatment. Step (6) of the algorithm can be further subdivided into several steps:

- 6a. determine the  $(x, y)$  coordinates of the points where the limb bud boundary intersects a vertical or horizontal grid line;
- 6b. determine the grid points that lie inside the limb bud domain;
- 6c. solve the advection–reaction–diffusion system.

Since the time steps for the fluid solver are small, we can use an explicit method in step (6c) for solving the advection–reaction–diffusion

system. Since we are only interested in the chemical concentrations within the limb bud boundary, we can ignore the solution at grid points outside of the limb bud. At regular grid points, we use the standard five point stencil in a central difference approximation to the Laplacian. Near the boundary, one or more of the grid points in the standard stencil will lie outside of the limb bud domain. At these irregular grid points, we make use of the Neumann boundary condition to develop an equation for the Laplacian approximation. If only one point is missing from the five-point stencil (Type 4), we use an approximation described in Morton & Mayers (1994). At irregular points with two (Type 3) or three points missing (Type 2), we assume that the limb bud boundary for the morphogen equations conforms to the grid lines. This gives us an  $O(h)$  approximation to the Laplacian on the perturbed boundary. The Type 4 solutions can be poor if the immersed boundary is very close to a grid point. Since our limb bud is growing, there are points that come arbitrarily close to the boundary. We circumvent the computational difficulty by assuming that the boundary is further away than it really is. While we lose some accuracy, the method is stable and inexpensive to compute. A more elegant approach based on the “immersed interface method” of LeVeque & Li (1994) could be incorporated into our numerical software.

### A.4. Determination of the Source Strength

At each time step, we must evaluate the local source strength  $S_{ij}^n$  at each mesh point.  $S_{ij}$  may depend on the local concentration of one or more growth factors  $c_{ij}^n$ . For the simulations shown in Section 4 and from eqn (41), the local source strength is given by  $S_{ij} = s_1(c_1)_{ij} + s_2$ . Mass balance over the entire fluid domain requires  $\sum_{i,j} S_{ij}^n = 0$ . The source terms within the fluid domain are balanced by four sinks located outside of the limb domain. We assume that  $S_{ij} = 0$  outside of the limb bud domain except at the sinks.